Collagen and Leather

RESEARCH Open Access

Polycaprolactone strengthening gelatin/nano-hydroxyapatite composite biomaterial inks for potential application in extrusion-based 3D printing bone scaffolds

Chenxin Wang[1], Mao Yang[2], Li Chen[1], Yijing Stehle[3], Mingyue Lin[1], Rui Zhang[1], Huanshuo Zhang[1], Jiehui Yang[1], Min Huang[4], Yubao Li[1*] and Qin Zou[1*]

Abstract

Extrusion-based three-dimensional (3D) printing of gelatin (Gel) is crucial for fabricating bone tissue engineering scaffolds via additive manufacturing. However, the thermal instability of Gel remains a persistent challenge, as it tends to collapse at mild temperatures. Current approaches often involve simply mixing Gel particles with various materials, resulting in biomaterial inks that lack uniformity and have inconsistent degradation characteristics. In this study, acetic acid was used to dissolve Gel and polycaprolactone (PCL) separately, producing homogeneous Gel/PCL dispersions with optimal pre-treatment performance. These dispersions were then combined and hybridized with nano-hydroxyapatite (n-HA) to create a composite printing ink. By evaluating the printability of the ink, the optimal conditions were identified: a n-HA concentration of 50% (w/w), a printing temperature of 10–15 ℃, a printing pressure of 2.5 bar, and a printing speed of 7 mm/s. The resulting biomaterial inks, with a composition of 25% Gel, 25% PCL, and 50% n-HA, demonstrated excellent printability and stability, along with significantly enhanced mechanical properties. As a result, 3D scaffolds with high printability and shape fidelity can be printed at room temperature, followed by deep freezing at -80 ℃ and cross-linking with vanillin. The Gel-based composite scaffolds demonstrated excellent biocompatibility, cell adhesion, cell viability and nano-hydroxyapatite absorption *in vitro*. Additionally, *in vivo* experiments revealed that the bioactive scaffold biodegraded during implantation and significantly promoted bone regeneration at the defect site. This provides a promising strategy for treating bone defects in clinical setting. In conclusion, the Gel/PCL/n-HA biomaterial inks presented here offer an innovative solution for extrusion bioprinting in the field of bone tissue engineering.

Keywords Gelatin, Nano-hydroxyapatite, Polycaprolactone, Polymer-matrix composites scaffold (PMCs), Bone regeneration

*Correspondence:
Yubao Li
nic7504@scu.edu.cn
Qin Zou
zouqin80913@126.com
Full list of author information is available at the end of the article

Graphical Abstract

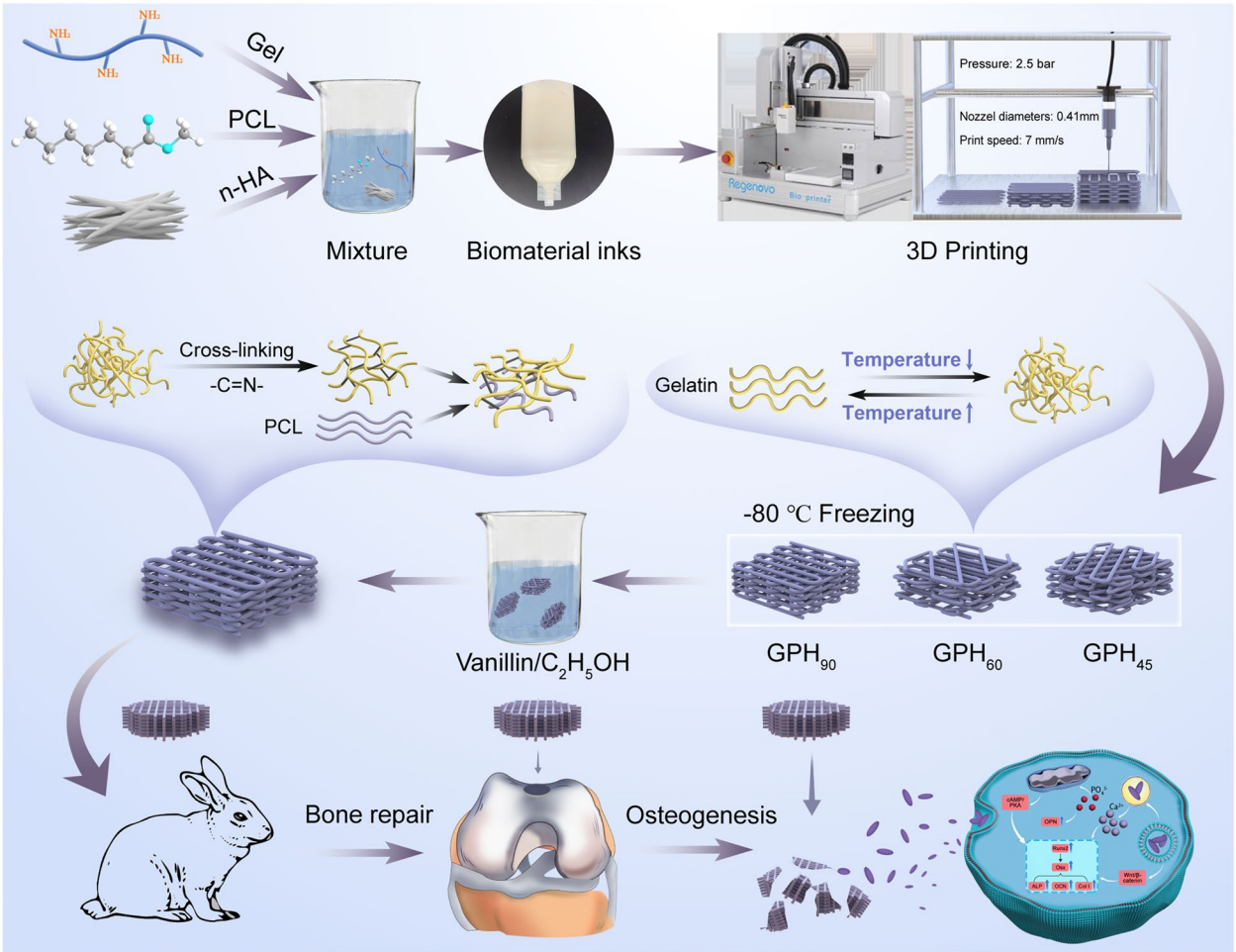

1 Introduction

Tissue engineering has become a clinical reality for the repair of various tissues, including cartilage, bone, liver, kidney, blood vessels, and skeletal muscle [1]. Extrusion bioprinting is widely used to fabricate complex and heterogeneous constructs for bone tissue engineering [2, 3]. In recent years, a range of 3D printable tools has been developed, with some now commercially available [4]. However, only a limited selection of biomaterials meets the necessary physicochemical criteria to serve as suitable 'inks' for printing [5]. Advancements in extrusion-based 3D printing for bone tissue engineering scaffolds rely heavily on the design of 3D printable biomaterials. Modern bone tissue engineering methods aim to use biomaterials that provide a biocompatible or even bioactive platform for tissue regeneration [6]. Despite significant progress, identifying qualified biomaterial inks remains challenging due to the conflicting requirements of printability, shape fidelity, and cell viability [7–9].

Bone tissue is a type of mineralized connective tissue primarily composed of calcium phosphate and type I collagen proteins [5, 10–12]. Gelatin (Gel), derived from collagen by breaking down its triple helical structure [11], is more hydrophilic and less immunogenic than collagen due to its increased reactive groups and reduced potential pathogens after degradation [13]. Additionally, Gel contains the specific cell adhesion sequence arginine-glycine-aspartic acid (RGD), which is the recognition site for integrins. This sequence plays a crucial role in regulating interactions between cells and the extracellular matrix (ECM), supporting bone tissue formation [14]. Some researchers have developed 3D printed Gel scaffolds with aperture diameters ranging from 400 to 800 μm, observing that the mechanical properties improved

with higher Gel solution concentrations [15]. Cells adhered and proliferated well within these Gel scaffolds. Further studies revealed that fibroblast growth accelerated when the pore size exceeded 580 μm and the porosity was greater than 83% [16]. Despite these advantages, extrusion-based 3D-printed Gel scaffolds have not been extensively studied. The use of Gel in biological scaffolds is limited by its low mechanical strength, rapid enzymatic degradation, and poor solubility at high concentrations. To enhance the mechanical properties, prolong degradation time, and broaden the applications of Gel, strategies such as crosslinking, chemical grafting, or blending Gel with other polymer materials are needed [16]. For example, methacrylated gelatin (GelMA) is a modified Gel that mainly consists of methacrylamide and methacrylate groups [17]. Despite its photoinitiated crosslinking characteristics, Gel faces significant challenges as printing ink, such as clogging and producing uneven, cracked scaffold fiber lines. To address these issues, 3D scaffolds combining Gel and alginate, can be enhanced with varying amounts of hyaluronic acid (HA) and nanohydroxyapatite (n-HA) for bone tissue engineering. However, this approach involves a two-step cross-linking process, which significantly complicates the preparation. Additionally, the problem of Gel's rapid degradation remains unresolved. Polycaprolactone (PCL), an FDA approved synthetic polymer, offers a promising solution. It is biocompatible, cost-effective, and has a relatively slow degradation rate, ranging from months to years [18]. PCL is soluble in many organic solvents, such as methylene chloride, making it suitable for extrusion-based 3D printing of scaffolds [19]. Integrating PCL can enhance the mechanical properties and longevity of Gel-based scaffolds, addressing key limitations in their application for bone tissue engineering. However, PCL often lacks cell-binding sites and is hydrophobic [20]. Additionally, its semi-crystalline nature results in a slow degradation rate taking over three years to fully degrade under *in vivo* conditions [21]. Therefore, it is essential to prepare a Gel/PCL dispersion with appropriate properties for 3D bioprinting, ensuring good printability and functionality.

In previous studies, Gel particles were uniformly dispersed into a PCL solution, and n-HA was added to prepare 3D printing ink. Compared to PCL/n-HA scaffolds, the composite scaffolds exhibited improved cell orientation effects and osteogenesis. In extrusion-based 3D printing, dichloromethane (DCM) is commonly used to dissolve PCL, serving as the main component of printing inks for creating bone tissue engineering scaffolds [22]. Unfortunately, Gel cannot be dissolved in DCM simultaneously with PCL, resulting in Gel existing in granular form within the PCL. PCL remains a single and independent polymer component when mixed with Gel and n-HA particles, which can result in the lack of uniformity in the biomaterial ink. PCL ($C_6H_{10}O_2$) is a semi-crystalline linear polymer, and its structural unit has 5 nonpolar methylene -CH_2 moieties and a polar ester -COO-. PCL is a polar polymer that can be dissolved in the polar solvent DCM [23]. When dissolved, the semi-crystalline PCL reaches a rubber state, and as DCM quickly evaporates, PCL rapidly cures during the 3D printing process [21]. In contrast, Gel, an amphoteric colloid, is insoluble in DCM, ethanol, ether, chloroform and most other nonpolar organic solvents, limiting its combination with PCL for extrusion 3D printing. Abdulah M. et al. reported the use of a formic/acetic acid mixed solvent to dissolve PCL, Gel, bacterial cellulose (BC), and n-HA, enabling the printing of a 3D multi-component hydrogel composite scaffold. Inspired by this, a new solvent system using acetic acid was designed for 3D printing ink. Acetic acid, being a greener chemical, produces rich carboxylic acid groups. PCL can be dissolved in acetic acid, and Gel, as an amphoteric colloid, is also soluble in acetic acid, glycerin, propylene glycol, and other polyol aqueous solutions. Therefore, it is feasible to dissolve both PCL and Gel in acetic acid for 3D printing applications.

In a typical extrusion-based printing procedure, a biomaterial ink is prepared in solution and extruded through a nozzle to form a filament. This filament is then deposited onto a collector plate, stacking to create a predesigned 3D shape while undergoing solidification, such as a sol-gel transition. At this stage, the ink must possess sufficient physical strength to maintain the shape of the filaments. Maintaining the shape of the filaments using only hydrogel biomaterials remains challenging. Bone, which comprises both organic and inorganic phases, originates from the ordered assembly of collagen fibers and hydroxyapatite nanocrystals [24]. To better meet the mechanical requirements, various inorganic biomaterials have been added to hydrogel biomaterial inks in recent years, significantly enhancing their performance [25]. Due to their similarity to the mineral phase of the human body, inorganic biomaterials such as n-HA, beta-tricalcium phosphate (β-TCP), and silicate bio-ceramics are known for their osteogenic and mineralization effects. Most biomaterial inks consist of natural or synthetic polymers with shear-thinning properties [26]. However, limited research has been conducted on assessing the use of Gel/PCL composite dispersion hybridized with n-HA to prepare composite printing ink.

In this research, we aim to present a novel Gel biomaterial ink for extrusion bioprinting, specifically for bone tissue engineering scaffolds. The biomaterial ink is based on Gel/PCL dissolved by acetic acid. The extrusion-based 3D printing ink involves creating an optimal PCL/Gel/n-HA dispersion with excellent processability. By analyzing

the printability of the ink, the most suitable n-HA concentration, printing temperature and other parameters were determined. Subsequently, 3D scaffolds with high printability and shape fidelity were printed in a room temperature atmosphere, followed by deep freezing at -80 ℃ and cross-linking with vanillin. Additionally, their printability with complex structures, *in vitro* biocompatibility, and *in vivo* osteogenic properties were evaluated, demonstrating their versatility and potential for widespread use in bone tissue engineering applications.

2 Materials and methods

2.1 Materials and reagents

Gel (type A, powder, gel strength ~ 300 g bloom) was purchased from Sigma Aldrich (China). PCL particles (average molecular weight approximately 80,000 g/mol; diameter approximately 2 mm) were purchased from Yisheng Co., Ltd. (Guangzhou, China). Sodium hydroxide (NaOH), sodium phorhoate tribaric dodecahydrate ($Na_3PO_4{\cdot}12H_2O$), and calcium nitrate terahydrate ($Ca(NO_3)_2{\cdot}4H_2O$) were purchased from Kelong Chemical Agent Co., Ltd. (Chengdu, China). Vanillin (Chron Chemicals Co., Ltd., China) was employed as a cross linker. All chemicals and reagents (acetic acid, absolute ethyl alcohol, etc., Chron Chemicals Co., Ltd., China) used in the experiments were analytical grade.

2.2 Development of 3D printing inks

2.2.1 Solubility analysis

In this study, a biomaterial ink formulation composed of Gel, PCL, n-HA, and acetic acid was proposed. By evaluating the solubility of Gel and PCL in acetic acid and the printability of the biomaterial inks, an optimal formula ratio was selected. This formulation was then used to prepare a porous multicomponent bio-nanocomposite scaffold using extrusion 3D printing technology. To determine the maximum concentration of the Gel/acetic acid and PCL/acetic acid solutions, five concentration gradients were designed (10%, 20%, 30%, 40%, and 50%). Gel and PCL solutions were prepared by dissolving the polymers under constant oscillation at 37 ℃ for 12 h. The maximum dissolved amounts of Gel and PCL were then identified and selected for further study.

2.2.2 Extrudability analysis

PCL/acetic acid solution was added to the Gel/acetic acid solution, and the mixture was stirred vigorously until a homogeneous paste was produced. Finally, 25%, 40%, and 50% (w/w) of n-HA were added and mixed thoroughly to obtain 3 kinds of Gel/PCL/n-HA 3D printing inks with different n-HA contents [27]. The extrudability was evaluated to determine the optimal biomaterial ink formula.

2.2.3 Printability experiments

The printability experiments (1D structures printing and 3D structures printing) were carried out while following the same conditions. The dimensions of the single layer reversed 'S' design were designed on 3D Max. The printed reversed 'S' structures were analyzed to evaluate the printability of biomaterial ink formulations after extrusion and to compare the similarity of the designed structure and control biomaterial inks.

2.3 Preparation of 3D printed Gel/PCL/n-HA (GPH) composite scaffolds

2.3.1 Model specification

Three kinds of microstructural scaffold models of [0°/ 90°/ 0°/ 90°] (GPH_{90}), [0°/ 60°/ 120°/ 0°/ 60°/ 120°] (GPH_{60}) and [0°/ 45°/ 90°/ 135°/ 0°/ 45°/ 90°/ 135°] (GPH_{45}) were designed using Perfactory RP software. In the design, the positive directions of the X and Y axes were 0° and 90°, respectively, with the Z axis representing the height adjustment direction. The crossing angles between fibers on adjacent layers were set to 90°, 60°, and 45° [28]. Cube scaffolds with a side length of 15 mm, a height of 6.5 mm, and a pore size of 1.5 mm, featuring interconnected 3D pores were designed. The layer height was set to 320 μm to ensure optimal deposition and adhesion between adjacent layers.

2.3.2 Fabrication of the scaffolds

Gel/PCL/n-HA 3D printing ink was filled into a 3D printing cartridge. Scaffolds were printed using an extrusion-based 3D bio-printer (Envisiontec 3D-bioplotter, Germany). The lattice scaffolds were fabricated by direct deposition through a tapered tip (0.41 mm). By adjusting the printing conditions (temperature and pressure), porous scaffolds with a three-dimensional structure were prepared. After printing, the Gel/PCL/n-HA scaffolds were stored at room temperature, 4 ℃, 0 ℃, -20 ℃ or -80 ℃ for 12 h. The scaffolds were cross-linked the next day in a 10% (wt) vanillin ethanol solution for 24 h at room temperature. The scaffolds were then thoroughly washed with purified water and dried in a vacuum oven (DZF-6090, China) at 37 ℃ for 2 ~ 3 h.

2.4 Characterizations of the 3D printed Gel/PCL/n-HA scaffolds

2.4.1 Morphological analysis

The pore size, pore shape, and general appearance of the composite scaffolds were characterized by stereoscopes (SMZ800N, Nikon, Japan). The surface morphology of the scaffolds was examined using the scanning electron microscope (SEM, Apreo S, Thermo Scientific, USA) at 20 kV. Samples for SEM examination were sputter-coated with gold before observation.

2.4.2 Physico-chemical characterization of scaffolds

The universal testing instrument (Auto-graph AG-IC 20/50KN, Japan) was used to characterize the compressive strength of three differently shaped scaffolds according to the protocol of GB/T 1041-92. A total of three specimens in each group with dimensions of 10 × 10 × 8 mm were measured at a compression speed of 1 mm/min.

The infrared spectra of samples were recorded on a Fourier transform infrared spectrometry (FTIR, Invenio R, Bruker, Germany). The raw materials of 3D printing were ground with KBr to prepare tablets employing a hydraulic press and the 3D printing ink was laid as a membrane. All spectra were recorded using reflectance mode (16 scans, scan range 500 – 3500 cm^{-1}, a resolution of 4 cm^{-1}). The phase composition and crystallinity of samples were analyzed by X-ray diffraction (XRD, PANalytical B. V., Empyrean, Netherlands). The X-ray diffractograms were recorded at 40 kV and 40 mA using Cu Kα in a 2θ range of 5 – 60° with a step of 0.026.

2.5 *In vitro* experiments

2.5.1 Cell culture

The human osteosarcoma (MG63) cells (a non-transformed cell line that exhibits an osteoblastic phenotype) were culture expanded in basal F-12 (Gibco, Life Technologies, USA) supplemented with 10% (v/v) newborn calf serum (NBCS, Gibco, Life Technologies, USA) and 1% (v/v) penicillin-streptomycin antibiotic solution (MP Biomedicals, USA) at 37℃ with 5% CO_2 [29]. The media was replaced every 2 – 3 days. Regular subculturing was performed using 0.25% trypsin-EDTA (Gibco, Life Technologies, USA). To evaluate the biological properties of the composite scaffolds *in vitro*, the adhesion and morphology of MG63 cells in direct contact with the scaffolds was primarily focused. Each specimen was sterilized with ethylene oxide gas. Cells cultured in media for 3 days were seeded at a density of 3×10^4 cells per specimen on the top of pre-wetted scaffolds, which were placed in the wells of a 24-well cell culture plate (Corning, USA). The cell/scaffold constructs were then cultured in a humidified incubator (37℃, 5% CO_2 and 90% humidity) for 4 and 7 days.

2.5.2 Cell morphology and attachment

For morphological analysis of the cell attached scaffolds, the samples were washed three times with PBS (PH = 7.4) after removing the medium and then fixed in 2.5% glutaraldehyde fixative (Solarbio, China) for 2h. Following thorough washing twice with PBS, the scaffolds were dehydrated using a graded series of tert-butanol (30%, 50%, 75%, 80%, 95%, and 100%) and then dried in a vacuum oven at a constant temperature of 37 ℃ overnight. Once properly dried, the samples were sputter-coated with gold and observed using a scanning electron microscope (SEM, Apreo S, Thermo Scientific, USA) at 20 kV.

At specified intervals, cells were washed with PBS (PH = 7.4) and fixed with 3.7% formaldehyde for 10 min at room temperature. After washing with PBS thrice, the cell-seeded scaffolds were stained with Alexa Flour ® 532 phalloidin (ex/em~531 nm/~554 nm, Invitrogen), Mitochondrion-Selective Probes (ex/em~490 nm/~516 nm, Mito Tracker®, Invitrogen) and Hoechst dyes (ex/em~350 nm/~461 nm, Invitrogen) for observing cell cytoskeleton, mitochondrion and nuclei, respectively. Cells were observed using Nikon confocal laser scanning microscopy (CLSM, Nikon A1R MP+, Japan).

Cell attachment and apatite entry into cells were characterized using transmission electron microscopy (TEM). Briefly, at the end of the incubation period, scaffolds with cells were harvested and washed three times with PBS (pH = 7.4). They were then fixed in 2.5% glutaraldehyde fixative (Solarbio, China) for 2 h. Subsequently, the samples were dehydrated using a gradient of acetone concentrations (30%, 50%, 70%, 80%, 90%, 95%, and 100%). Each concentration was applied for 15 min, and the dehydration using 100% acetone was repeated three times. The samples were treated with three penetrant mixtures 3:1 (v/v) mixture, of dehydrant and phenolic epoxy resin (Epon 812) for 30–60 min, 1:1 (v/v) mixture of dehydrant and phenolic epoxy resin for 30–60 min, and then a penetrant 1:3 (v/v) mixture of dehydrant and phenolic epoxy resin for 30–60 min. The permeated samples were embedded and heated to prepare embedded samples. Ultra-thin slices (70–90 nm) were obtained using the Leica EM UC7. The sections were stained with lead citrate solution and 50% saturated uranium acetate solution for 15–20 min [30]. The sliced samples were mounted on copper meshes and observed using the Tecnai G2 F20 S-TWIN transmission electron microscope (TEM).

2.6 *In vivo* experiment

2.6.1 Surgical procedure

3D printed Gel/PCL/n-HA (GPH_{90}, GPH_{60}, GPH_{45}) scaffolds (Φ5 mm × 6 mm) were sterilized by ethylene oxide. The surgical procedures were conducted following the ethical protocols approved by the Ethics Committee of the West China Animal Experiment Center of Sichuan University. Nine New Zealand white rabbits weighing between 2.3 and 2.50 kg, comprising both male and female rabbits, were randomly divided into three groups, with three rabbits in each group. Anesthesia was induced using pentobarbital sodium at a dosage of 20 mg/kg of body weight. The distal femur was exposed by making an incision through the skin and dissecting through the layers of fascia, muscle, and periosteum. A cylindrical bone defect (Φ5 mm × 6 mm) was created in the trochlear

groove of the distal femur using an electric drill. The incision was then sutured layer by layer. Following the surgery, each rabbit received intramuscular injections of penicillin (1×10^5 units per day) for 3 days. Implants were harvested for further characterization at 4-, 8-, and 12-weeks post-surgery.

2.6.2 Micro-CT imaging and histological examination

At 4-, 8-, and 12-weeks post-surgery, the rabbits were euthanized, and their femurs containing the scaffold implants were harvested. The samples were fixed with a fixative and scanned using microcomputed tomography (micro-CT, Viva CT80, SCANCO Medical AG, Switzerland), from which 3D reconstructed images of the new bone tissue were obtained. A threshold of 220–280 was applied to distinguish the scaffold materials, while a threshold of 280–1000 was applied to distinguish bone tissue. A cylindrical region with a diameter of 5 mm was selected at the center of the implanted scaffold area, and the 3D reconstructed images of the new bone tissue were acquired from approximately 300 axial images. The osteogenesis on and within the porous scaffolds was evaluated using the direct method software integrated with the micro-CT, based on the obtained 3D reconstructed images.

2.6.3 Histological examination

The samples were decalcified embedded in paraffin and sectioned into slices with a thickness of 5 μm. The sections were stained with hematoxylin and eosin (H&E) and Masson trichome and finally observed using an optical microscope (TE 2000-U Nikon, Japan).

2.7 Statistical analysis

Statistical analysis was carried out using the mean ± standard deviation (SD). The analysis of variance (ANOVA) was used to determine the statistical significance among different groups. A p value < 0.05 was considered statistically significant.

3 Results and discussion

3.1 Biomaterial ink preparation and characterization

Printability, a crucial parameter in evaluating extrusion-based 3D printing inks, depends significantly on ink viscosity. This viscosity is influenced by factors such as temperature, ink composition, and component content during bioprinting [31]. Initially, the optimal solution concentrations for both polymers were determined through a gradient sweep (Fig. 1A). Gel powders and PCL particles were dissolved in acetic acid at various ratios (10%, 20%, 30%, 40%, 50%; w/v) under constant agitation (37 ℃ for 12 h). At concentrations of 10%, 20%, and 30%, both Gel and PCL dissolved completely: the Gel/acetic acid solution appeared as a yellow transparent liquid, while the PCL/acetic acid solution was colorless and transparent. However, at concentrations of 40% and 50%, the Gel powders and PCL particles were not completely dissolved (□). The viscosity of the polymer solution increased with both Gel and PCL concentration. To ensure optimal printability of the biomaterial inks and avoid issues caused by low viscosity, the maximum dissolved amounts of Gel and PCL (30%) were selected for subsequent experiments. Compared with other PCL/Gel/BC/n-HA composite scaffolds, the concentration of PCL and Gel was improved substantially (from 14% to 30%) [32].

The physical gelling of the biomaterial ink formulations and the extrusion conditions were evaluated to determine the optimal component composition at which the hydrogels should be printed (Fig. 1B). The free-flowing behavior of the solutions indicated poor gelation, while a rigid gel indicated that physical gelling had occurred [7]. Specifically, the solutions of Gel/acetic acid, PCL/acetic acid and Gel/acetic acid + PCL/acetic acid flowed to the liquid level (marked by the orange dotted line) in parallel to the horizontal plane when the bottle was inclined, indicating poor fidelity. As the amount of n-HA increased, the liquid level gradually became parallel to the bottom of the glass bottle, indicating improved fidelity. Extrudability refers to the capability to extrude the ink through a nozzle to form a continuous and controllable filament. Generally, the extrusion of ink from nozzles can be characterized in one of four cases: (a) un-extrudable, (b) un-continuous (or jetting), (c) continuous yet uncontrollable, or (d) continuous and controllable [33]. By adjusting the printing parameters, three types of solutions were extruded and their flow characteristics were investigated. Gel has high elasticity, causing it to clog the needle and prevent printing when pressure is applied (cyan arrow). PCL ink showed good flowability and could be extruded uniformly with slight pressure. However, the fidelity of the PCL ink was poor, it could not maintain its shape after extrusion. When PCL was mixed with Gel, it failed to extrude into slender and uniform filaments. To address these challenges, n-HA, an inorganic biomaterial similar to the mineral phase of human bone, was added to the Gel/PCL composite solution. The addition of n-HA increased the viscosity of the biomaterial ink and facilitated gel formation, ultimately furnishing optimal printing performance at 50% n-HA (green arrow). This addition also enhanced the stiffness of the biomaterial ink by reducing the elasticity of the Gel.

Temperature and the addition of inorganic materials are crucial parameters affecting viscosity in 3D printing. Typically, viscosity increases with the amount of ceramic filler and decreases with temperature. Researchers have

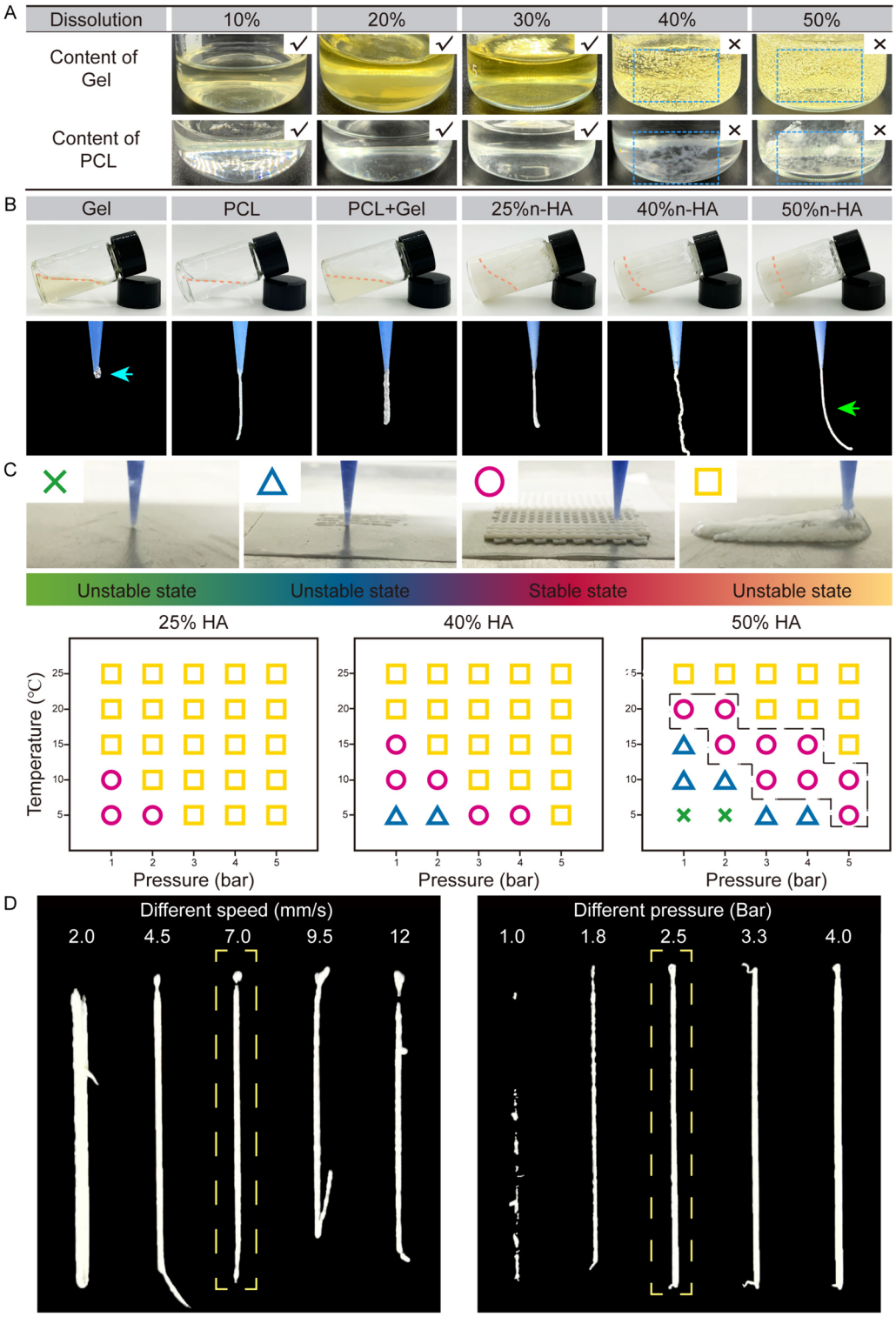

Fig. 1 Printability of Gel/PCL/n-HA biomaterial inks. **A** Dissolution of Gel/acetic acid and PCL/acetic acid at different concentrations. **B** Gelling and extrusion condition of the biomaterial inks at different component compositions. The orange dotted line illustrates the surface level of the material in the sample bottle. **C** Printability profiles of inks with different n-HA contents whereas the green error symbol (✕) indicates that the needle is blocked. The blue triangle (△) indicates difficulties in smooth extrusion, the red circle (○) denotes smooth extrusion of the ink, and the yellow square (□) signifies inability to form extrusion. The green, blue, and yellow colors represent an unstable state, and the red color indicates a stable state. **D** Screening the optimal printing rate and printing pressure. The yellow dotted box signifies the optimal printing condition

developed methods to assess the printability range, categorized by symbols representing printability errors (green), unstable printing (triangles in blue), stable printing (circles in red), and non-printing (squares in yellow) [34]. Through comparative analysis of ink printability profiles with varying n-HA contents under different pressure and temperature conditions, it was found that the ink containing 50% n-HA exhibited the most stable behavior. This concentration was optimal for producing binder fibers and achieving fully stacked layers in the printed scaffolds.

To meet the rheological requirements for solid filament formation during the extrusion process, the printing ink should turn from a sol status to a proper gel status when being extruded from the printing ink cavity onto the printing platform. The Gel is a temperature-sensitive material and is subjected to reversible sol-gel phase transition upon temperature elevation to room temperature. When the temperature surpasses the gel point of Gel, it begins to dissolve, leading to a decrease in viscosity, which is unfavorable for subsequent extrusion molding. From further analysis of the printing ink with 50% n-HA content, the most suitable printing temperature range was determined to be 10–15 ℃.

Further, the viscosity of the inks determines the pressure and speed required for extrusion. Appropriate process parameters ensure the fabrication of well-defined filaments, while mismatched biomaterial ink viscosity and process parameters can lead to irregular filaments. Based on previous research findings regarding printing pressure, it was hypothesized that the optimal pressure was 3 bar and the corresponding optimal printing speed was then ascertained. As depicted in Fig. 1D, when the printing speed was too slow (e.g., 2 mm/s), excess ink accumulated in one spot, resulting in filament diameters larger than the set value. Conversely, when the printing speed was too fast (e.g., 12 mm/s), the extruded ink couldn't deposit completely on the receiving plate, causing filament breakage. After determining the optimal printing speed, the corresponding optimal printing pressure was then determined. Ultimately, the optimal conditions were established at a linear speed of 7 mm/s and a printing pressure of 2.5 bar.

3.2 Evaluation of printability and 3D construct formation

The development of 3D printing ink should focus on systematically evaluating methods to achieve structures with high fidelity, resolution, and accuracy. Key factors affecting the transition from printing lines in 1D to printing 3D structures must be carefully considered. Figure 2A illustrates the shapes of printed lines with acute angles (45°), right angles (90°), and obtuse angles (120°) under identical parameters. Currently, printing quality is poorer with acute angles compared to obtuse and right angles, often resulting in overlapping issues. In this study, this problem was addressed by adjusting printing process parameters such as air pressure and speed (blue arrow). This adjustment minimized ink accumulation at acute angle corners, resulting in smooth, robust filaments across all three angles with high fidelity and no collapse.

The aim of analyzing the printed reversed 'S' structures was to effectively observe the dimensional accuracy and consistency exhibited by the biomaterial ink formulations with respect to the dimensions of the designed structure (Fig. 2B1-B4). The degree of similarity of the printed construct with the intended design is referred to as printing accuracy. The dimensions of the single-layer reversed 'S' designed created in 3D Max consisted of three long lines, each 15 mm in length, connected by two 5 mm short lines at opposite ends (Fig. 2B1). Analysis of the lengths (L) and widths (S), as well as the start and end points of Gel/PCL/n-HA biomaterial ink formulations, determined the printability outcomes. Throughout the printing process, there was only a minor initial discrepancy (yellow dotted line), the rest of the print path however followed the computer designed trajectory. After the printing process, there was no excessive material deposition (red circle). In high-magnification images, the material was uniformly extruded at corners (B3) and straight lines (B4), forming filaments of consistent width. The structural integrity of the biomaterial ink filaments was tested by printing a continuous line over pillars with predefined gaps of 18, 10, 6, 4, and 3 mm (Fig. 2B5).

Since bone is a complex 3D structure that provides mechanical support, to design an ideal scaffold for bone-tissue regeneration, one must consider the optimum mechanical properties of the scaffold. The mechanical property is a function of both the material's inherent elastic modulus and the scaffold's architecture. Therefore, the mechanical properties of porous scaffolds can be tailored by altering their architecture. In this study, three kinds of microstructural scaffold models of [0°/90°/0°/90°], [0°/60°/120°/0°/60°/120°] and [0°/45°/90°/135°/0°/45°/90°/135°] were designed using Perfactory RP software (Fig. 2C-path design). The positive directions of the X and Y axes were set at 0° and 90°, respectively, while and the Z axis controlled the vertical adjustments [35]. The angles at which fibers crossed between adjacent layers were 90°, 60°, and 45°. Following the completion of the design phase, Gel/PCL/n-HA scaffolds were fabricated layer by layer using an extrusion-based 3D printer. The pore size and interconnected porosity were critical factors in scaffold design. Increasing porosity can reduce mechanical strength but is essential for facilitating cell migration, proliferation, nutrient diffusion, oxygen availability for cell viability, and scaffold vascularization [36]. Studies

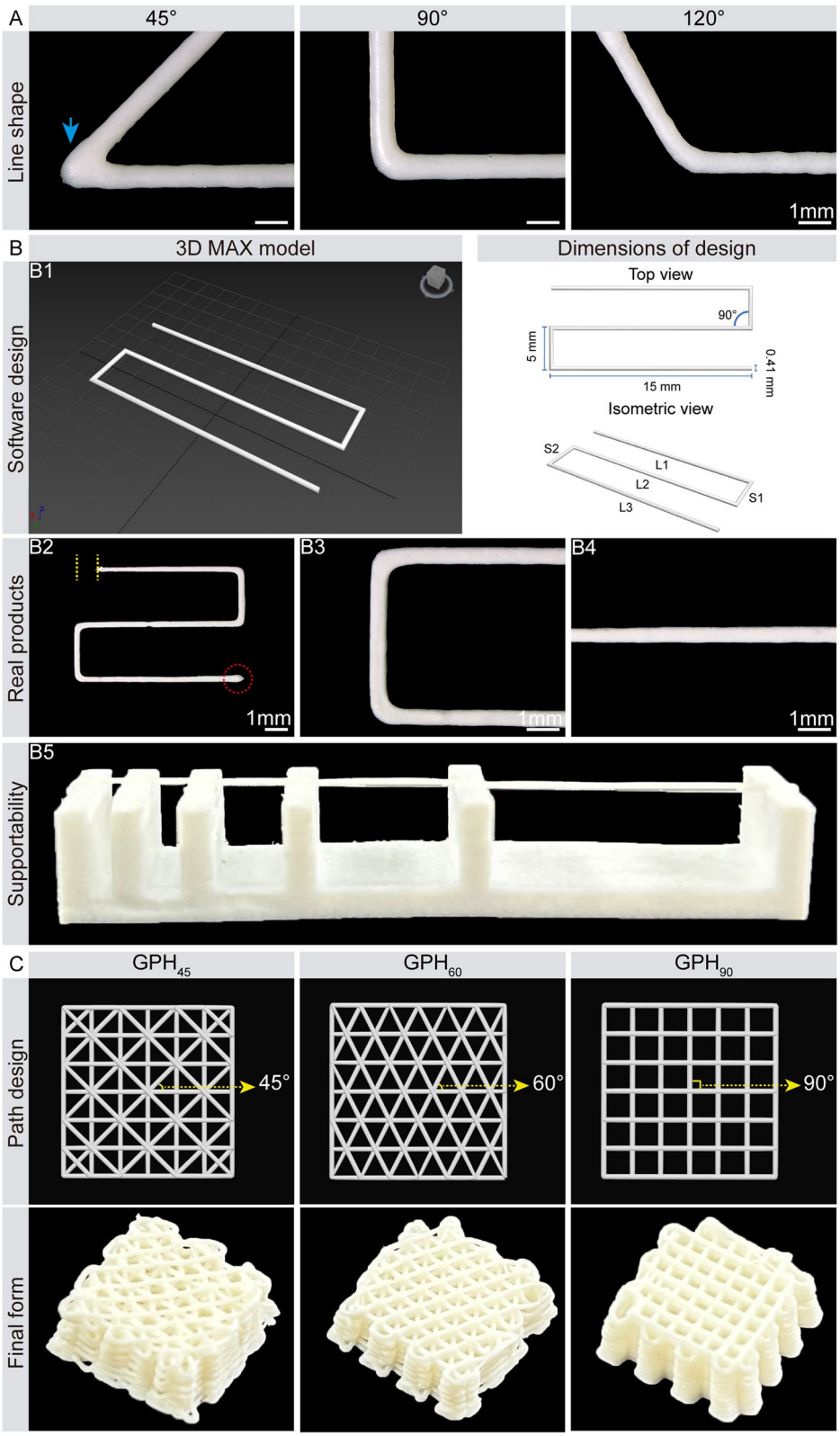

Fig. 2 High-fidelity 3D printing of Gel/PCL/n-HA ink. **A** Line shape of acute, right, and obtuse angle printing. Blue arrow: the stack in the corner. **B** Reversed 'S' design, (B1) 3D design as seen in 3D Max, and representation of dimensions of the design. (B2-B4) Photographs showing printed reversed 'S' design. Yellow dotted line: missing part. Red dotted circle: deposition of material. (B5) Bracing stability of printing filament. **C** Final form of 3 kinds of scaffolds (GPH_{45}, GPH_{60}, GPH_{90})

indicate that implants with apertures > 300μm exhibit superior osteogenic effects [37]. Based on relevant studies and considerations specific to the printing process, cubic scaffolds were designed with dimensions of 15 mm side length, 6.5 mm height and a pore size of 1.5 mm, featuring interconnected three-dimensional pores [38]. Ultimately, three types of 3D scaffolds (GPH_{45}, GPH_{60}, GPH_{90}) were successfully fabricated (Fig. 2C-final form).

3.3 Curing and formation of GPH scaffolds

Similar to A. Kumar's study [39], the results from this study showed that the freshly fabricated completed GPH scaffolds gradually collapsed at room temperature, lost the through-hole structure, and dissolved during water immersion (Fig. 3①). Inspired by the work of A. Kumar [39], the GPH scaffolds were cured by freezing (4 ℃, 0 ℃, -20 ℃ and -80 ℃) to prevent the collapse. After being frozen for 12 h, the GPH scaffolds dissolved upon soaking in water at room temperature, causing them to lose their 3D shape (Fig. 3②). The Gel dissolves in aqueous solutions. Crosslinking enhances both the thermal and mechanical stability of the Gel. The current research demonstrated that vanillin aldehyde, used as a crosslinking agent, is non-toxic and biocompatible. After freezing, the scaffolds were crosslinked with vanillin in an ethanol solution. The overall process is illustrated in Fig. 3. Ultimately, scaffolds frozen at 4 ℃, 0 ℃, and -20 ℃ collapsed in water at room temperature (Fig. 3③), whereas only the scaffolds frozen at -80 ℃ maintained stability for more than 3 days (Fig. 3④).

First, GPH scaffolds in a natural environment were prepared by extrusion-based 3D printing. Infrared spectra of acetic acid, PCL, Gel, and n-HA (Fig. 4(a)) showed characteristic patterns of newly printed GPH scaffolds, which included the symmetric and asymmetric vibration of the $-CH_2$ group at 2943 cm^{-1} and 2865 cm^{-1} [40]. The peak at 1721 cm^{-1} was assigned to the C=O bonds of the ester group, while the peak at 1162 cm^{-1} was assigned to -C-O-C- asymmetric stretching [41]. There was a characteristic peak of Gel at 1643 cm^{-1}, attributed to amide I (C=O stretching), and another peak at 1540 cm^{-1} corresponding to amide II (N-H and $-CH_2$). Further, characteristic absorption peaks from PO_4^{3-} groups in the n-HA crystals were observed at 1026 cm^{-1}. Acetic acid, as the solvent, exhibited its characteristic peak at 1700 cm^{-1}. Common chemical reactions among organics are substitution reactions, addition reactions, elimination reactions, polymerization reactions and redox

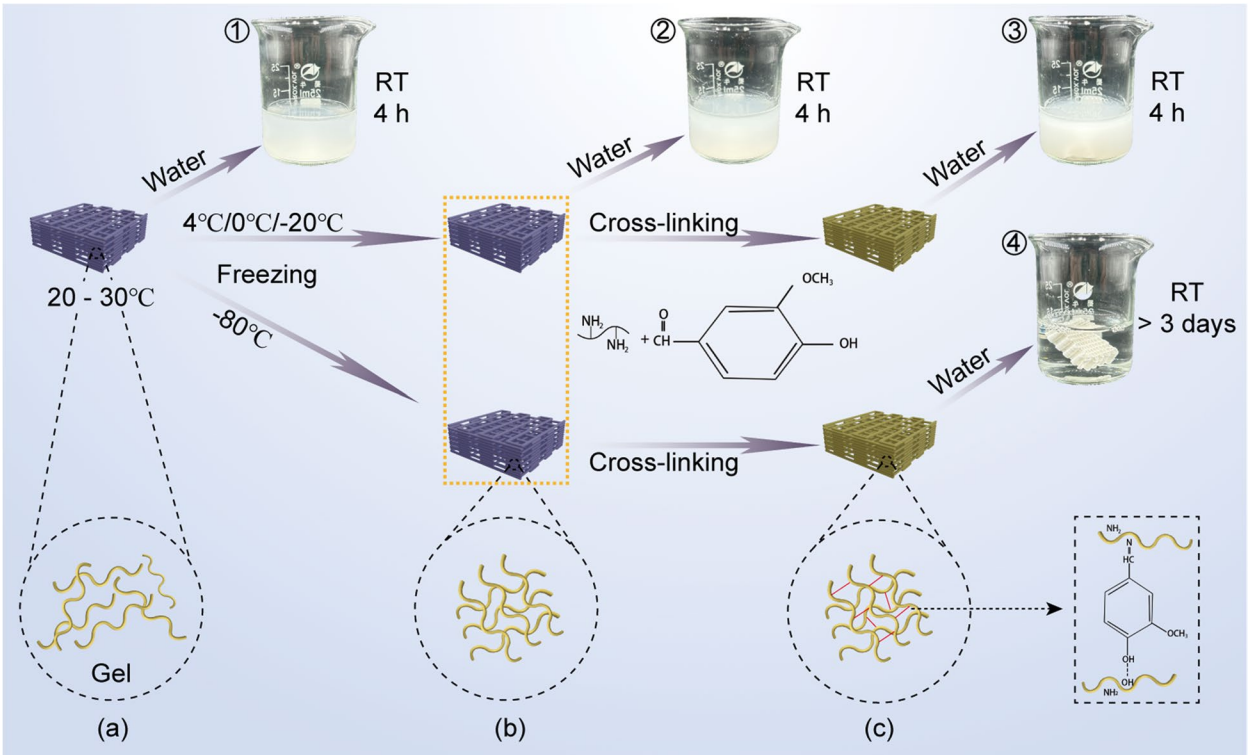

Fig. 3 Schematic diagram representing freezing and cross-linking of GPH scaffolds (**a**) Distribution of Gel's molecular chains at room temperature (RT: 20–30 ℃). **b** Molecular chains of Gel following freezing. **c** Molecular chains of Gel following vanillin crosslinking. ①-④: State of GPH scaffolds (obtained through different cross-linking conditions) after soaking in water

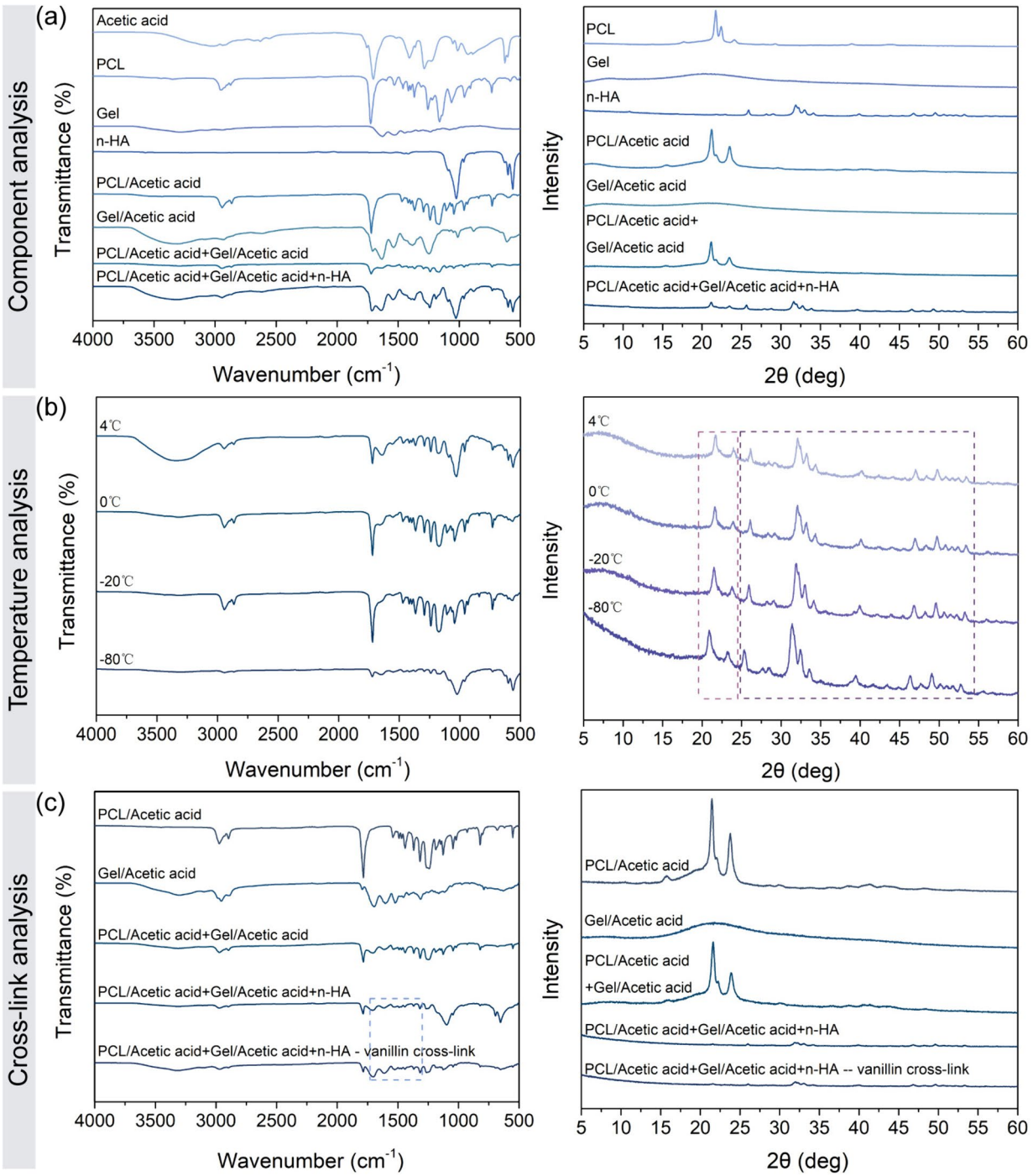

Fig. 4 FTIR and XRD graphs of GPH scaffolds at different stages. **a** Freshly fabricated 3D scaffolds. **b** Scaffolds after being frozen at different temperatures. **c** Scaffolds after cross-linking by vanillin

reactions. Since the side chain of the PCL molecular chain consists mainly of stable -CH_2 groups, all experimental processes occurred under normal temperature and pressure conditions. Furthermore, Gel dissolved in acetic acid only changed its three-dimensional conformation without affecting the molecular chain. Hence, no chemical reaction occurred between Gel and PCL, as confirmed by FTIR showing their characteristic peaks. The XRD patterns of the 3D printed ink revealed the crystal structure of PCL, with characteristic peaks observed at 2θ = 21.2°, 21.9°, and 23.6° corresponding to the (110), (111), and (200) planes, respectively.

For n-HA, peaks appeared at 2θ = 26.3° and 31.6°, corresponding to the (002) and (211) crystal planes [42]. In contrast, Gel displayed no crystalline peaks but exhibited a broad halo peak, indicating its amorphous structure. PCL is a semi-crystalline polymer, while hydroxyapatite adopts a hexagonal crystal system structure, explaining the observed crystallization characteristics in the XRD pattern.

Similar to the spectra of the 3D printing ink material at room temperature, scaffolds cured at different low temperatures (4 ℃/0 ℃/-20 ℃/-80 ℃) (Fig. 4(b)) showed the characteristic peaks of each component at 2943 cm^{-1} (symmetric vibration of the -CH_2), 2865 cm^{-1} (the asymmetric vibration of -CH_2), 1634 cm^{-1} (amide I), 1540 cm^{-1} (amide II) and 1026 cm^{-1} (PO_4^{3-}), which implied that no changes have been introduced in the composition of the scaffold during freezing [43].

Meanwhile, the XRD patterns of the scaffolds at various low temperatures consistently exhibited the characteristic peaks of each component of the printing ink, indicating that the crystal structure of each component remained unchanged following freezing treatment. The gel is a thermo-reversible cross-linking material capable of maintaining its stable structure at low temperatures. This cross-linking is purely physical and does not involve the formation of new chemical bonds [34]. Consequently, the frozen scaffolds dissolved upon immersion in water.

The thermal cross-linking of Gel was reversible, necessitating additional chemical cross-linking to stabilize its structure. Vanillin's aldehyde group can react with Gel's amino group through a Schiff base reaction. The chemical structure of the cross-linked scaffolds was analyzed using FTIR spectra (Fig. 4(c). Besides the characteristic peaks of each scaffold component, absorption peaks at 1651 cm^{-1} and 1586 cm^{-1} appeared, indicating the formation of the Schiff base structure (orange dashed square) between Gel's amino group and vanillin's aldehyde group [44]. XRD analysis showed that the crystallization of the scaffolds remained largely unchanged after vanillin cross-linking, with all characteristic peaks of each component present. Subsequent immersion of the vanillin-cross-linked scaffolds in water showed that only those frozen at -80 ℃ did not dissolve. This may be attributed to the closer proximity of Gel molecular chains at -80 ℃ resulting in a denser Gel molecular network after thermal and vanillin cross-linking, which was less susceptible to water-induced degradation.

3.4 Characterization of 3D printed GPH composite scaffolds after cross-linking

Based on macroscopic observation, the scaffolds exhibited a clear pore structure characterized by interlaced and interpenetrating filaments without adhesion or collapse (Fig. 5A1-A3). When viewed from the side, it was evident that all three types of scaffolds were formed layer by layer. Subsequently, the dried scaffolds were examined using a stereoscope (A4-A6). All scaffolds displayed uniform structures with interconnected macro-scale pores, averaging approximately 1000 μm in size. The scaffold surfaces appeared granular, with some small pores visible (A5, cyan arrow). Under SEM, the filament diameters of all scaffolds fell mainly within the range of 200–300 μm. The surfaces of the filaments exhibited uneven pores (A7), likely due to the volatilization of acetic acid during processing. The relatively rough structure was attributable to aggregates of n-HA embedded within the filaments. These micropores can provide a suitable site for the growth and multiplication of cells. The presence of such microporous structures is prevalent in 3D solvent-printed scaffolds containing powder mixtures.

PCL is synthesized through the ring-opening polymerization of the cyclic monomer ε-caprolactone and the presence of methylene groups in its molecular chain makes PCL less hydrophilic [45]. The hydrophilicity of various materials was assessed by forming them into films. PCL/DCM is commonly used as an extrusion-based 3D printing ink, with a water contact angle (WCA) of 77.15° ± 2.33°. The hydrophobic nature of PCL (WCA: 77.97° ± 1.11°) remained unchanged even when using acetic acid as the solvent. The Gel is a macromolecular hydrophilic polymer. Its molecular structure contains a large number of -OH, -COOH, and -NH_2, groups which make Gel extremely hydrophilic [41]. Compared with PCL, the hydrophilicity of the composite material was greatly improved by adding Gel (WCA: 70.91° ± 1.87°). In addition, the hydrophilicity of PCL was also improved following the addition of n-HA (WCA: 53.66° ± 1.03°). This is due to the presence of hydrophilic -OH and Ca^{2+} in n-HA [42]. The improved hydrophilicity of scaffold material provided a good environment for the growth and adhesion of cells and bone tissues.

The mechanical properties of scaffolds with different three-dimensional structures were assessed through compression testing (Fig. 5C, D). The GPH_{45} scaffold failed to form a stable triangular structure, with four filaments intersecting at the same fulcrum. Consequently, the compressive stress of the GPH_{45} scaffold group (7.57 ± 0.25 MPa) was significantly lower than that of the GPH_{60} (13.23 ± 0.14 MPa) and GPH_{90} (11.41 ± 0.45 MPa) scaffold groups (p<0.01) [46]. The hexagonal shape of the GPH_{60} scaffold provided a regular triangular pore structure, resulting in good structural stability [47]. However, in the GPH_{60} scaffold, three filaments converged at a single fulcrum, exerting greater pressure on the fulcrum compared to the GPH_{90} scaffold. This led to no significant difference in compressive strength between the

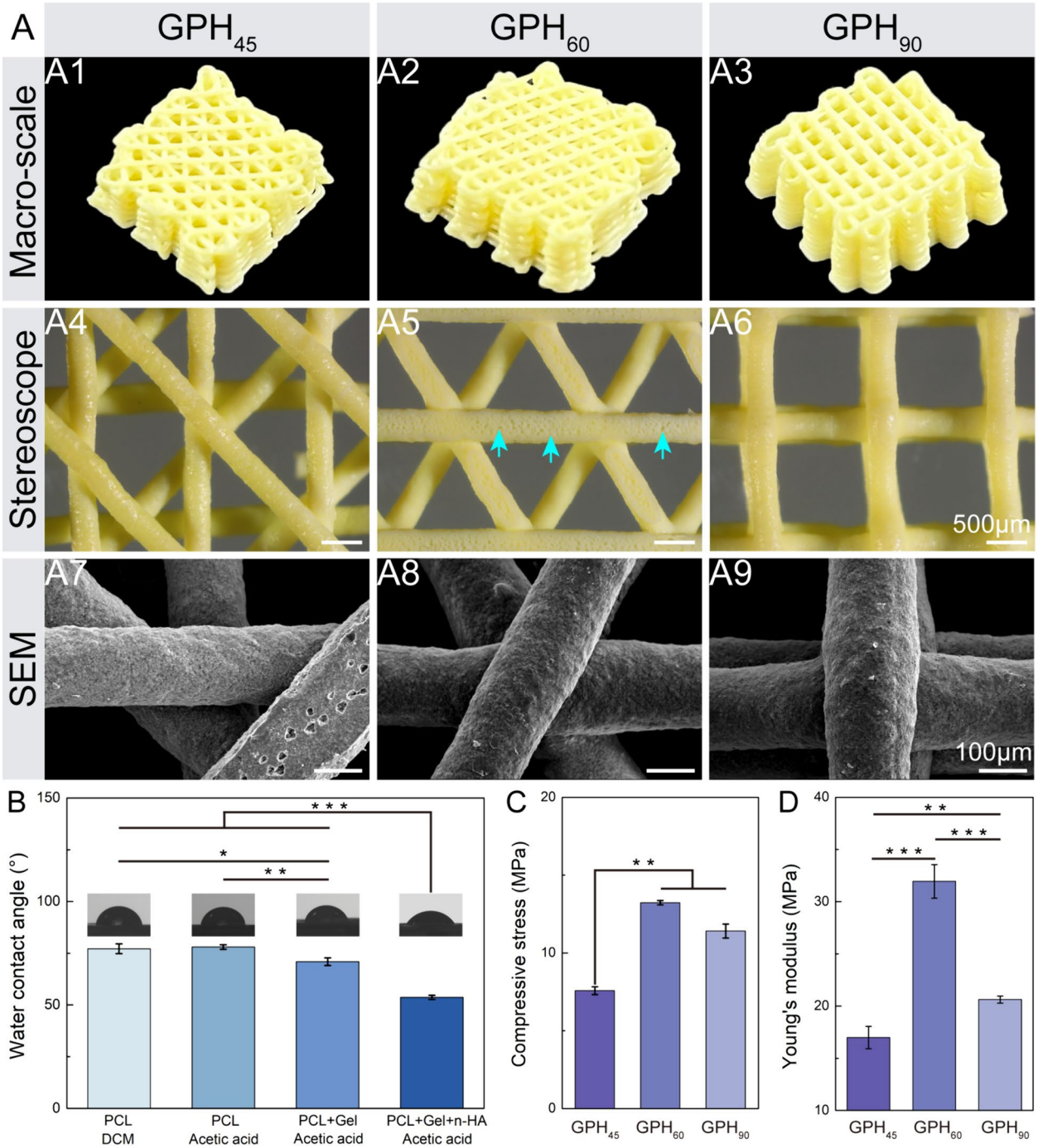

Fig. 5 **A** Digital photograph, stereoscopic images, and SEM micrographs of three different kinds of GPH scaffolds following cross-linking. **B** The water contact angle (WCA) of various scaffolds composition. **C** Compressive stress and (**D**) Young's modulus of three different 3D structured scaffolds (Error bars: mean ± SD ($n = 3$), *$p < 0.05$, **$p<0.01$, ***$p < 0.01$)

GPH_{60} and GPH_{90} scaffolds. Young's modulus is a physical quantity that describes the resistance of a solid material to deformation and is measured as the stiffness of the scaffolds. The Young's modulus of the scaffolds showed that GPH_{60} (31.95 ± 1.61 MPa) was significantly higher than GPH_{45} (16.98 ± 1.07 MPa) and GPH_{90} (20.62 ± 0.35 MPa). The stable triangular structure of the GPH_{60} scaffold provided superior stiffness and the mechanical benefits of this structure outweighed the adverse effect of the three filaments sharing one fulcrum. It can be seen that

the structural changes caused by the structures alone can lead to differences in the mechanical properties of the scaffolds.

3.5 *In vitro* cytocompatibility of composite scaffolds

SEM (A1-A2) and CLSM (B1-B4) results confirmed the attachment and proliferation of MG63 cells on the scaffold surfaces. All scaffold components being non-toxic, cells adhered and grew well on the scaffold surface. SEM images showed well-distributed cells exhibiting various morphologies, including spindle-shaped, triangular, and polygonal forms [48]. Figure 6A1 showed a large number of cells effectively adhering to the scaffold structure, covering the edges of the walls [49]. The cells grew flat and aligned in parallel along the scaffold filaments, forming a cell layer. The high-magnification image (A2) showed that individual cells were plump and spindle-shaped. Meanwhile, the cells explored their surroundings using filopodia and spikes, with numerous filopodia extending from the cell bodies and connecting to surface materials (yellow arrow). Confocal microscopy staining visualized the migration and proliferation of cells on the GPH scaffolds. MG63 cells cultured on the composite scaffolds were fluorescently stained to identify actin (red), mitochondria (green), and nuclei (blue). After co-culturing with the GPH scaffolds, the cells spread across a large area with long, net-like lamellipodia. Almost all cells stretched out, showing actin filaments attaching to the scaffold surface and aligning parallel to the scaffold filaments (B1) [50]. In Fig. 6B2, numerous irregular holes (10-30 μm in diameter) on the scaffold filaments were observed, with surrounding cells growing into the scaffold and actin clinging to the edges of these holes [51]. At the intersection between the scaffold layers (B3), cells climbed up along the filament direction, growing from the lower layer to the upper layer. The high-magnification image (B4) showed diffuse and brightly stained nuclei (blue) on the scaffolds' surface. The abundance of mitochondria (green) indicated strong cell viability on the scaffolds. The cytoskeleton, supporting the entire cell structure, displayed spindle-shaped, triangular, or polygonal forms, highlighted by F-actin staining in red. These findings suggest that the scaffolds effectively support cell adhesion and proliferation. Cell adhesion is primarily influenced by specific ligand interactions between the cells and the scaffolds. Chemically, the composition of the scaffold materials significantly affects their performance [52]. Gel, a hydrolysis product of collagen, contains bioactive sequences such as the RGD peptide, which integrins on MG63 cells can recognize and bind to [53]. Moreover, the contact angle measurements revealed that the addition of Gel and n-HA significantly improved the hydrophilicity of PCL, reducing the contact angle from 77.97° ± 1.11° to 53.66° ± 1.03° (Fig. 5B). Studies indicate that surface hydrophilicity with contact angle values between 40° and 70° optimally supports cell adhesion and migration on the scaffold [54].

In a previous study, the TEM micrographs of the n-HA-Tb nanocrystals implanted in new bone tissue were observed, and the change in their uniform morphology and size with implantation time was noted [55]. n-HA-Tb nanocrystals showed uniform rod-like morphology and n-HA type crystal structure. In Fig. 6C1-C2, some "black particles" with irregular morphology were found to be evenly distributed in the matrix of the scaffold materials. The uniform rod-like morphology of these "black particles" strongly suggested their identity as n-HA, as indicated by previous studies and n-HA's presence as a component within the scaffolds. In Fig. 6C1, MG63 cells were tightly bound to the scaffold matrix, and a large number of mitochondria and endoplasmic reticulum structures could be seen [56]. Mitochondria (yellow triangle) located near the rough endoplasmic reticulum (white arrow) exhibited characteristic double membranes with granule-free cristae [57]. Intracellular granules typically gain access through one of three pathways: pinocytosis, receptor-mediated pinocytosis, and phagocytosis. [57]. Due to the higher phase activity of n-HA, it readily enters cells via phagocytosis. TEM images showed a close interaction between n-HA released from scaffolds and cells, followed by internalization via endocytosis pathways. Various stages of n-HA degradation were observed after it entered the cell through endocytosis and formed vesicles (①-④). Overall, GPH scaffolds exhibited good cytocompatibility, providing sites for cell adhesion and promoting cell proliferation on its surfaces.

3.6 Degradation and osteogenesis of 3D scaffolds *in vivo*

Three types of scaffolds were implanted into the defected area of the rabbits' trochlear femoris (Fig. 7A) to evaluate their degradation and osteogenesis abilities *in vivo*. All the animals survived until the conclusion of the study, and no complications occurred during the perioperative period. Clinical and macroscopic evaluations revealed no signs of necrosis or infection before bone sample retrieval. Through the 3D reconstruction and combination of 3 groups scaffolds and the distal femur, the micro-CT images showed that the structure of the scaffolds in each group was maintained quite well, and all of them showed a cylindrical morphology (Fig. 7B). More details were observed through 2D images (Fig. 7C). At 4 weeks post-surgery, the implanted scaffolds (GPH_{45}, GPH_{60}, GPH_{90}) still filled almost the entire defect area. The distinct stacking patterns of the three scaffold groups (0°/45°/90°/135°, 0°/60°/120°, 0°/90°) were visible in the 2D images. By 8 weeks, the overall shape and

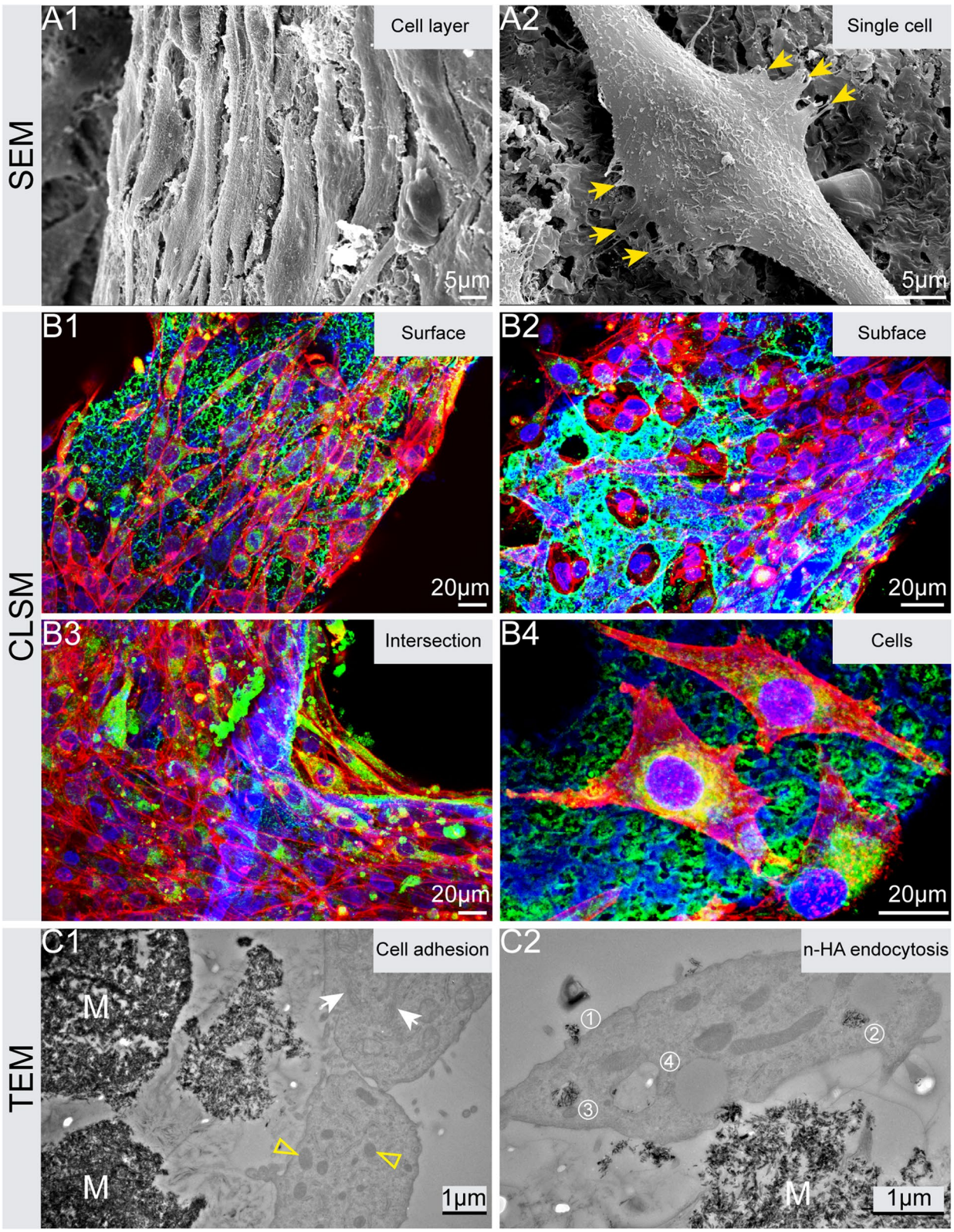

Fig. 6 *In vitro* cytocompatibility of GPH scaffolds. (A1-A2) SEM micrographs of MG63 cells co-cultured with scaffolds. (B1-B4) CLSM images. Blue: nucleus labeled by Hoechst dyes. Green: mitochondria labeled by the MitoTracker® probes. Red: actin labeled by phalloidin. (C1-C2) TEM micrographs of MG63 cells adhesion and n-HA endocytosis (M: material, white arrow: rough endoplasmic reticulum, yellow triangle: mitochondria)

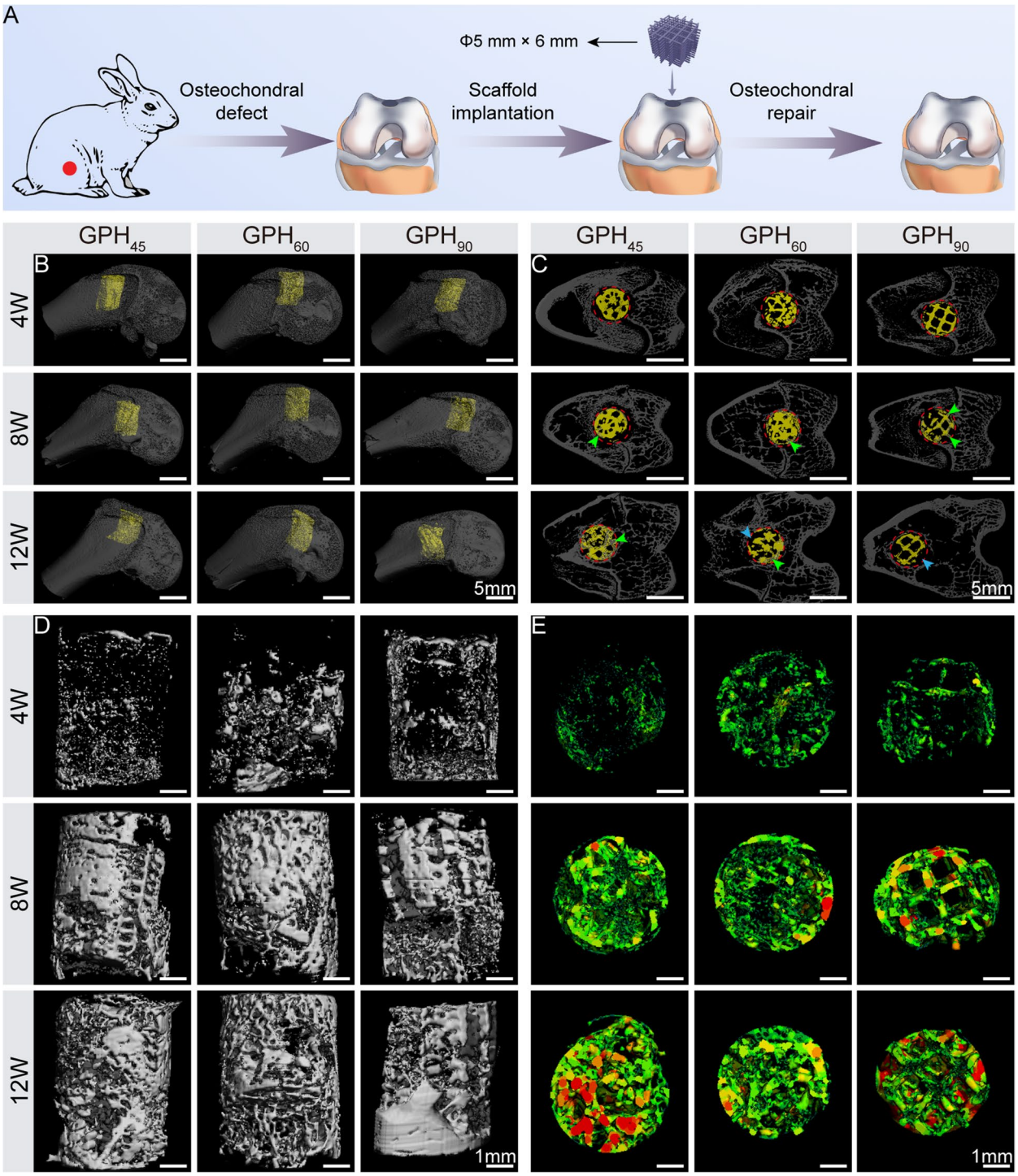

Fig. 7 Micro-CT results of scaffold degradation and bone repair experiments. **A** Schematic diagram representing scaffold implantation in rabbits' trochlea femoris. **B** Three-dimensional (3D) reconstruction images of the distal femur and composite scaffolds (yellow) in the defect area. **C** Two-dimensional (2D) cross-sectional image. The red circle represents the defect area. **D** Bone regeneration (4, 8, 12 W) in the defect area after 3D reconstruction. **E** Visualization of the trabecular thickness of new bone in the defect area. The color mapping indicated that the higher degree of red color correlated with the higher thickness of the trabecular bone

porous structure of the scaffolds remained mostly intact, with only mild degradation at the periphery, accompanied by new trabeculae forming around the scaffold (green arrow) [58]. At 12 weeks, the scaffolds continued to degrade from the outside inwards (blue arrow), with increased bone regeneration. Several porous structures were still visible, although the distinct morphology had gradually become blurred.

Next, 3D reconstruction of new bone tissue in the defect area was performed to evaluate the bone regeneration ability of the composite scaffolds (Fig. 7D). At 4 weeks post-surgery, the amount of new bone in each group was minimal, with new bone tissue forming only a thin layer around the defect [59]. By the 8th week, the amount of new bone had increased compared to the 4th week, extending not only over the surface of the bone defect but also growing to a certain depth along the scaffold. At 12 weeks, high-density bone appeared on the defect surface, and the peripheral bone tissue gradually thickened. There was almost no space between the bone trabeculae, and the newly formed bone tissue was dense. The newly generated bone within the defects was reconstructed in three dimensions at each time point, with the bone trabeculae thickness indicated by different colors (Fig. 7E). The thickness of the bone trabeculae at the periphery of the defects increased over time in all three groups. From 4 to 8 weeks, the bone trabeculae gradually grew inward from the periphery of the defect along the scaffold. After 8 to 12 weeks, part of the trabecula thickened and changed color from green to red. The above results demonstrated the good stability and osteogenic potential of GPH composite scaffolds.

3.7 Histological analysis

Hematoxylin and eosin (H&E) staining were used to analyze the inflammation and degradation of implanted GPH scaffolds (Fig. 8). Following 4 weeks of implantation, all scaffolds maintained their original structure and formed a tight bond at the bone-implant interface [60]. High-magnification images revealed a certain degree of inflammation around the early implanted scaffolds. This was attributed to the residual acetic acid from scaffold degradation, which created a weakly acidic environment *in vivo*, leading to localized inflammation. The H&E images showed that most inflammatory cells were concentrated around the scaffold materials (yellow arrow). As the scaffold gradually degraded, the acetic acid was absorbed, leading to a decrease in inflammatory cells around the scaffolds and a subsequent weakening of the inflammatory response. Due to the presence of five hydrophobic $-CH_2$ moieties in its repeating units, PCL exhibited the slowest degradation rate among all the polyesters [61]. Arif et al. have indicated that PCL exhibited stability within the living body and did not show any considerable degradation for six months and the material took two years for complete degradation [22]. However, the degradation rate of the Gel was faster *in vivo*. *In vivo*, matrix metalloproteinases-2 (MMP-2, gelatinase A) and MMP-9 (gelatinase B) can degrade Gel, allowing the degradation rate of the scaffold to be controlled by adjusting the Gel content. In this study, the addition of Gel resulted in significant scaffold degradation observed at 8 weeks, enhancing the degradation rate of PCL. The GPH_{45} and GPH_{90} groups exhibited more blank areas, indicating a higher degree of degradation.

The new and mature bone matrix has been shown in blue and red respectively following Masson trichrome staining Fig. 9 [62]. At 4 weeks, new bone in all three scaffold groups was in direct contact with the cancellous bone at the scaffold-original bone interface [63]. The porous structures of the scaffolds enhanced osteoconductivity. Osteoblasts were observed around the scaffold materials (green arrow), and numerous blue collagen fibers grew into the defect through the scaffold pores (ex: GPH_{90} – 4W). The red area of the tissue section increased and the color deepened over time, meaning the bone tissue at the interface between the scaffold and the original bone gradually matured for 8 weeks [64]. A mass of osteoblasts appeared around the scaffold, and collagen fibers grew into the defect area, wrapping the materials. By the 12th week, the new bone tissue around the scaffold had matured further, changing from blue to red. The *in vivo* results showed that the scaffold was tightly bound to the surrounding native bone tissue, indicating that n-HA on the scaffold surface promoted bone integration. Additionally, the bone architecture was random with an elaborate interconnected porous structure, allowing for nutrient transport and cellular ingrowth [65]. In the early stages of scaffold implantation, the three groups of scaffolds featured many lateral pore structures, guiding a large number of collagen fibers to grow inward. Over time, the bone tissue around the scaffold gradually matured, and the bond between the new bone and the materials strengthened. By the 12th week, mature new bone tissue had begun to appear inside the scaffolds.

To sum up, PCL provided mechanical support for the 3D printing scaffold in this study due to the presence of repeating hexanoate entities that give it excellent stiffness, mechanical elasticity, thermal stability, rheology, and viscoelasticity. Gel, due to the existence of Arg-Gly-Asp (RGD)-like sequence, promoted cell adhesion and migration, and was beneficial to bone cell recruitment for the 3D scaffold [66]. As the primary inorganic component of human bones, n-HA offers excellent stability, biocompatibility, and controlled degradation. It enhanced osteoblast adhesion and proliferation,

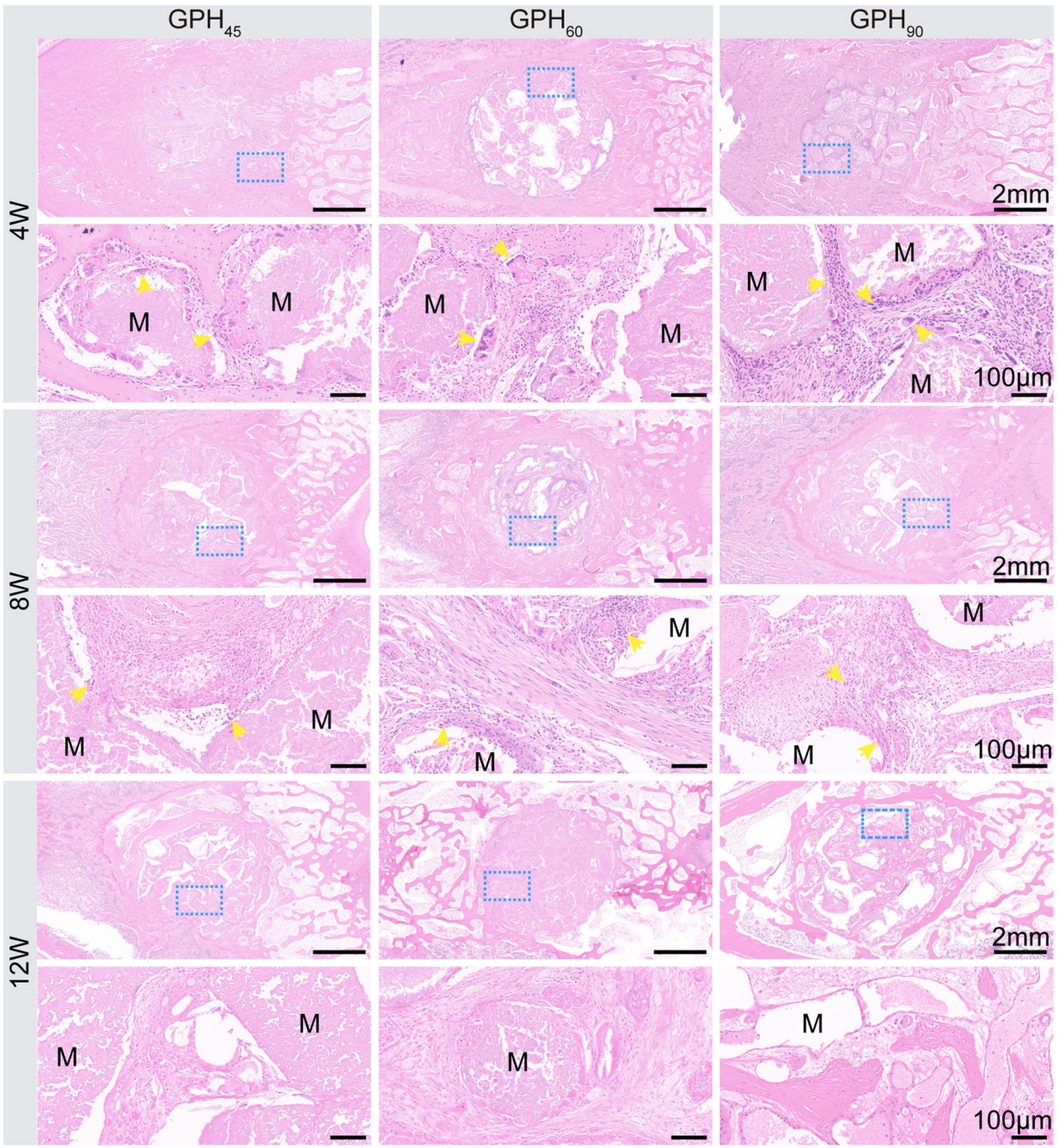

Fig. 8 Histological analysis of distal femur transverse section following scaffold implantation. H&E staining results of the 3 groups at 4, 8, and 12 weeks. The image below is a magnification of the blue square in the image above. Yellow arrows indicate inflammatory cells. M represents scaffold materials

facilitated the secretion of the extracellular matrix, and formed chemical bonds with natural bone. Based on the above results, the Gel/PCL/n-HA 3D printing ink formulation effectively promotes bone defect healing, confirming its potential for use in bone tissue engineering scaffold production.

4 Conclusion

In conclusion, composite biomaterial inks Gel/PCL/n-HA were successfully synthesized via dissolution in acetic acid. The printability of the ink was analyzed, and the optimal n-HA concentration, printing temperature, and other parameters were experimentally determined.

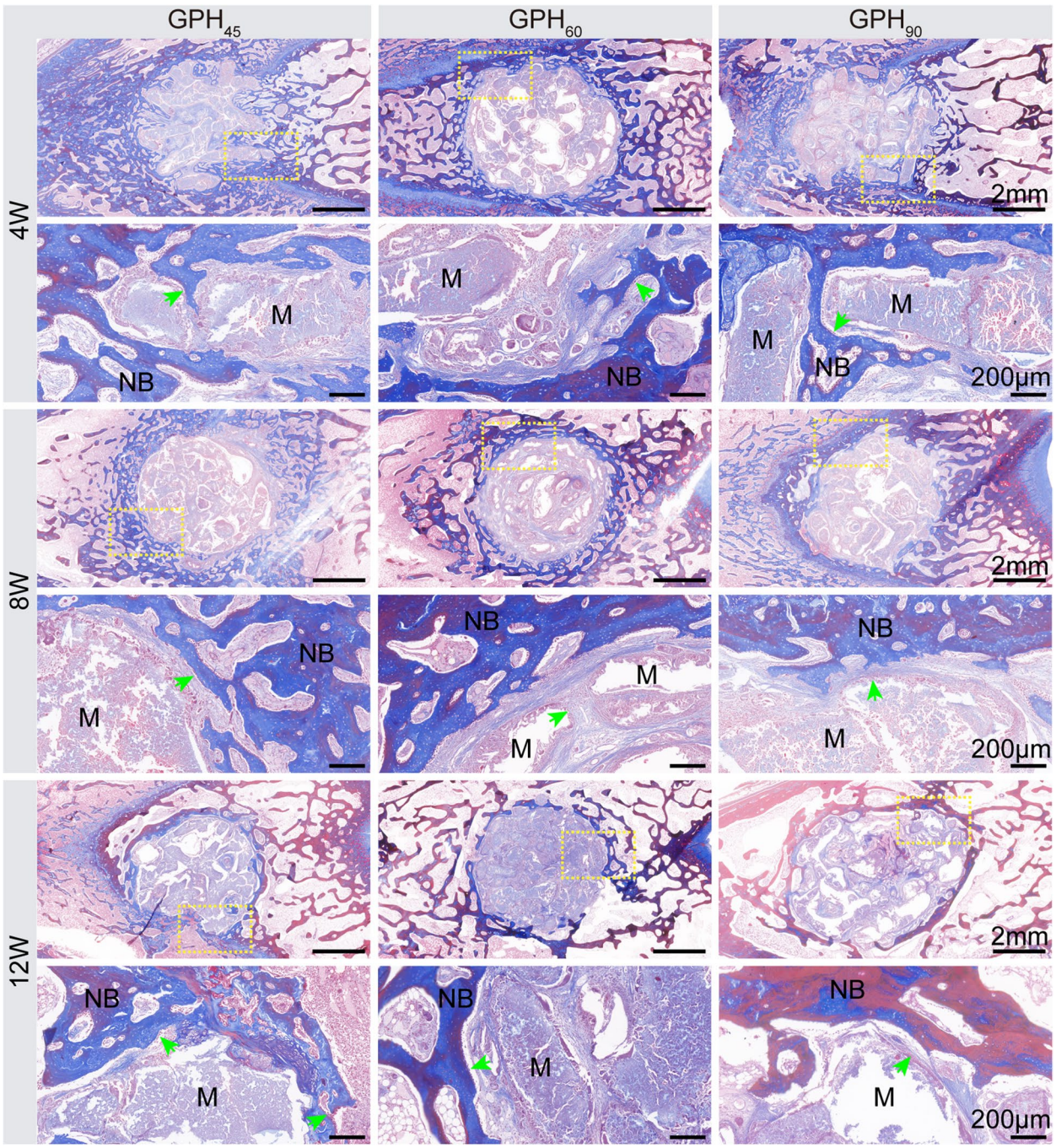

Fig. 9 Masson trichome staining results of the 3 groups at 4, 8, and 12 weeks. The image below is a magnification of the yellow square in the image above. Green arrows indicate osteoblast. NB means new bone

Following printing, the scaffolds were frozen at -80 °C and cross-linked with vanillin to stabilize them. Biocompatibility testing *in vitro* affirmed their ability to promote cell proliferation and spreading. Furthermore, application in rabbit calvaria defects demonstrated their reparative function in bone healing. It was indicated by our study that the Gel/PCL/n-HA biomaterial ink could be considered an excellent choice for extrusion-based printing, with significant potential for biological and clinical applications, particularly in bone tissue engineering.

Abbreviations

PSM	Polymer-matrix composites scaffold
Gel	Gelatin
PCL	Polycaprolactone
n-HA	Nano-hydroxyapatite
GPH	Gel/PCL/n-HA scaffold
HA	Hyaluronic acid
RGD	Arginine-glycine-aspartic acid
ECM	Extracellular matrix
GelMA	Methacrylated gelatin
DCM	Dichloromethane
β-TCP	Beta-tricalcium phosphate
BC	Bacterial cellulose
FTIR	Fourier transform infrared spectrometry
XRD	X-ray diffraction
SEM	Scanning electron microscope
CLSM	Confocal laser scanning microscopy
TEM	Transmission electron microscopy
H&E	Hematoxylin and eosin

Acknowledgments
We would like to thank Guiping Yuan and Shanling Wang at the Analytical & Testing Center of Sichuan University for their help with TEM analysis.
We would like to thank Lei zhang at the school of cyber science and engineering of Sichuan University for his support in data analysis using Cyber space virtual simulation experiment teaching platform.

Authors' contributions
Chenxin Wang: conceptualization, methodology, investigation, writing – original draft, and writing – review and editing. Mao Yang: investigation and methodology. Li Chen: resources investigation and project administration. Yijing Stehle: resources investigation and project administration. Mingyue Lin: investigation and methodology. Rui Zhang: investigation and methodology. Huanshuo Zhang: investigation and methodology. Jiehui Yang: investigation and methodology. Min Huang: resources investigation and project administration. Yubao Li: conceptualization, methodology, writing – review and editing, and funding acquisition. Qin Zou: conceptualization, methodology, writing – review and editing, and funding acquisition.

Funding
This work was supported by the National Key Research and Development Program of China [No. 2021YFA1201300], Innovation and Reform Project of Postgraduate Education of Sichuan University in 2021 and Analysis and Test Technology Innovation Project of Analytical & Testing Center.

Availability of data and materials
All data generated or analyzed during this study are included in this published article.

Declarations

Ethics approval and consent to participate
The animal study was approved by the Ethical Committee of Sichuan University (20230317009). The surgical procedures were performed following the ethical protocols of the Ethics Committee of West China Animal Experiment Center of Sichuan University.

Competing interests
The authors declare that they have no known competing financial interests or personal relationships that could have appeared to influence the work reported in this paper.

Author details
[1]Analytical & Testing Center, Sichuan University, Chengdu 610064, P. R. China. [2]Sichuan University Wangjiang Hospital, Sichuan University, Chengdu 610064, P. R. China. [3]Department of Mechanical Engineering, Union College, 807 Union St, Schenectady, NY 12308, USA. [4]Sichuan Institute of Atomic Energy, Chengdu 610101, P. R. China.

Received: 13 March 2024 Revised: 22 June 2024 Accepted: 27 June 2024
Published online: 01 September 2024

References

1. Chen Z, Cai Z, Zhuang P, Li F, Cui W, Li Z. Living probiotic biomaterials for osteoporosis therapy. Biomedical Technology. 2023;1:52–64.
2. Cui H, Yu Y, Li X, Sun Z, Ruan J, Wu Z, et al. Direct 3D printing of a tough hydrogel incorporated with carbon nanotubes for bone regeneration. J Mater Chem B. 2019;745:7207–17.
3. Du C, Hu J, Wu X, Shi H, Yu HC, Qian J, et al. 3D printing of a tough double-network hydrogel and its use as a scaffold to construct a tissue-like hydrogel composite. J Mater Chem B. 2022;103:468–76.
4. Zhu Y, Kong B, Liu R, Zhao Y. Developing biomedical engineering technologies for reproductive medicine. Smart Medicine. 2022;1(1):e20220006.
5. Yang B, Liu H, Jiang L, Zeng Y, Han Y, Sha C, et al. 3D bioprinting of collagen-based materials for oral medicine. J Leather Sci Eng. 2023;5(1):1–19.
6. Liu C, Xu X, Cui W, Zhang H. Metal-organic framework (MOF)-based biomaterials in bone tissue engineering. Engineered Regeneration. 2021;2:105–8.
7. Ren X, Wang J, Wu Y, Zhang Y, Zhang J, Bai L, et al. One-pot synthesis of hydroxyapatite hybrid bioinks for digital light processing 3D printing in bone regeneration. J Mater Sci Technol. 2024;188:84–97.
8. Yu X, Jiang S, Li D, Shen SGF, Wang X, Lin K. Osteoimmunomodulatory bioinks for 3D bioprinting achieve complete regeneration of critical-sized bone defects. Compos Part B-Eng. 2024;273:111256.
9. Zhang B, Belton P, Teoh XY, Gleadall A, Bibb R, Qi S. An investigation into the effects of ink formulations of semi-solid extrusion 3D printing on the performance of printed solid dosage forms. J Mater Chem B. 2024;121:131–44.
10. Sun L, Li S, Yang K, Wang J, Li Z, Dan N. Polycaprolactone strengthening keratin/bioactive glass composite scaffolds with double cross-linking networks for potential application in bone repair. J Leather Sci Eng. 2022;4:1.
11. Peng F, Zhang X, Wang Y, Zhao R, Cao Z, Chen S, et al. Guided bone regeneration in long-bone defect with a bilayer mineralized collagen membrane. J Leather Sci Eng. 2023;5:36.
12. Chen Q, Pei Y, Tang K, Albu-Kaya MG. Structure, extraction, processing, and applications of collagen as an ideal component for biomaterials - a review. J Leather Sci Eng. 2023;5:20.
13. Yuan L, Li X, Ge L, Jia X, Lei J, Mu C, et al. Emulsion Template Method for the Fabrication of Gelatin-Based Scaffold with a Controllable Pore Structure. ACS Appl Mater Interfaces. 2018;111:269–77.
14. Cui Y, Zhu T, Li A, Liu B, Cui Z, Qiao Y, et al. Porous Particle-Reinforced Bioactive Gelatin Scaffold for Large Segmental Bone Defect Repairing. ACS Appl Mater Interfaces. 2018;108:6956–64.
15. Dong J, Ding H, Wang Q, Wang LA. D-Printed Scaffold for Repairing Bone Defects. Polymers. 2024;16(5):706.
16. Choi DJ, Park SJ, Gu BK, Kim Y-J, Chung S, Kim C-H. Effect of the pore size in a 3D bioprinted gelatin scaffold on fibroblast proliferation. J Industr Eng Chem. 2018;67:388–95.
17. Liu J, Li L, Suo H, Yan M, Yin J, Fu J. 3D printing of biomimetic multi-layered GelMA/nHA scaffold for osteochondral defect repair. Materials & Design. 2019;171:107708.
18. Mouser VHM, Abbadessa A, Levato R, Hennink WE, Vermonden T, Gawlitta D, et al. Development of a thermosensitive HAMA-containing bio-ink for the fabrication of composite cartilage repair constructs. Biofabrication. 2017;9(1):015026.
19. Kim S, Kim J, Gajendiran M, Yoon M, Hwang MP, Wang Y, et al. Enhanced Skull Bone Regeneration by Sustained Release of BMP-2 in Interpenetrating Composite Hydrogels. Biomacromolecules. 2018;1911:4239–49.
20. Li J, Wang C, Gao G, Yin X, Pu X, Shi B, et al. MBG/ PGA-PCL composite scaffolds provide highly tunable degradation and osteogenic features. Bioact Mater. 2022;15:53–67.
21. Wang S, Gu R, Wang F, Zhao X, Yang F, Xu Y, et al. 3D-Printed PCL/Zn scaffolds for bone regeneration with a dose-dependent effect on osteogenesis and osteoclastogenesis. Mater Today Bio. 2022;13:100202.

22. Arif ZU, Khalid MY, Noroozi R, Sadeghianmaryan A, Jalalvand M, Hossain M. Recent advances in 3D-printed polylactide and polycaprolactone-based biomaterials for tissue engineering applications. Int J Biol Macromol. 2022;218:930–68.
23. Raucci MG, D'Anto V, Guarino V, Sardella E, Zeppetelli S, Favia P, et al. Biomineralized porous composite scaffolds prepared by chemical synthesis for bone tissue regeneration. Acta Biomater. 2010;610:4090–9.
24. Sawadkar P, Mohanakrishnan J, Rajasekar P, Rahmani B, Kohli N, Bozec L, et al. A Synergistic Relationship between Polycaprolactone and Natural Polymers Enhances the Physical Properties and Biological Activity of Scaffolds. ACS Appl Mater Interfaces. 2020;1212:13587–97.
25. Wang J, Wu D, Zhang Z, Li J, Shen Y, Wang Z, et al. Biomimetically Ornamented Rapid Prototyping Fabrication of an Apatite–Collagen–Polycaprolactone Composite Construct with Nano–Micro–Macro Hierarchical Structure for Large Bone Defect Treatment. ACS Appl Mater Interfaces. 2015;747:26244–56.
26. Li C, Cui W. 3D bioprinting of cell-laden constructs for regenerative medicine. Engineered Regeneration. 2021;2:195–205.
27. Zhou X, Sun J, Wo K, Wei H, Lei H, Zhang J, et al. nHA-loaded gelatin/alginate hydrogel with combined physical and bioactive features for maxillofacial bone repair. Carbohydr Polym. 2022;298: 120127.
28. Cakmak AM, Unal S, Sahin A, Oktar FN, Sengor M, Ekren N, et al. 3D Printed Polycaprolactone/Gelatin/Bacterial Cellulose/Hydroxyapatite Composite Scaffold for Bone Tissue Engineering. Polymers (Basel). 2020;12(9):1962.
29. Dwivedi R, Kumar S, Pandey R, Mahajan A, Nandana D, Katti DS, et al. Polycaprolactone as biomaterial for bone scaffolds: Review of literature. J Oral Biol Craniofac Res. 2020;101:381–8.
30. Ahmed MK, Zayed MA, El-Dek SI, Hady MA, El Sherbiny DH, Uskokovic V. Nanofibrous epsilon-polycaprolactone scaffolds containing Ag-doped magnetite nanoparticles: Physicochemical characterization and biological testing for wound dressing applications *in vitro* and *in vivo*. Bioact Mater. 2021;67:2070–88.
31. Brunel LG, Christakopoulos F, Kilian D, Cai B, Hull SM, Myung D, et al. Embedded 3D Bioprinting of Collagen Inks into Microgel Baths to Control Hydrogel Microstructure and Cell Spreading. Adv Healthc Mater. 2024;2303325.
32. Cakmak AM, Unal S, Sahin A, Oktar FN, Sengor M, Ekren N, et al. 3D Printed Polycaprolactone/Gelatin/Bacterial Cellulose/Hydroxyapatite Composite Scaffold for Bone Tissue Engineering. Polymers. 2020;2(9):1962.
33. Fu Z, Naghieh S, Xu C, Wang C, Sun W, Chen X. Printability in extrusion bioprinting. Biofabrication. 2021;13(3):033001.
34. Yin J, Yan M, Wang Y, Fu J, Suo H. 3D Bioprinting of Low-Concentration Cell-Laden Gelatin Methacrylate (GelMA) Bioinks with a Two-Step Crosslinking Strategy. ACS Appl Mater Interfaces. 2018;10(8):6849–57.
35. Liu H, Qiu L, Liu H, Li F, Fan Y, Meng L, et al. Effects of Fiber Cross-Angle Structures on the Mechanical Property of 3D Printed Scaffolds and Performance of Seeded MC3T3-E1 Cells. ACS Omega. 2021;649:33665–75.
36. Lee SS, Du X, Kim I, Ferguson SJ. Scaffolds for bone-tissue engineering Matter. 2022;59:2722–59.
37. Karageorgiou V, Kaplan D. Porosity of 3D biomaterial scaffolds and osteogenesis. Biomaterials. 2005;2627:5474–91.
38. Sarkar N, Bose S. Liposome-Encapsulated Curcumin-Loaded 3D Printed Scaffold for Bone Tissue Engineering. ACS Appl Mater Interfaces. 2019;1119:17184–92.
39. Kumar A, Brown RA, Roufaeil DB, Gupta A, Lipford EL, Muthusamy D, et al. DeepFreeze 3D-biofabrication for Bioengineering and Storage of Stem Cells in Thick and Large-Scale Human Tissue Analogs. Adv Sci. 2024;11(11):e2306683.
40. Singh RK, Jin G-Z, Mahapatra C, Patel KD, Chrzanowski W, Kim H-W. Mesoporous Silica-Layered Biopolymer Hybrid Nanofibrous Scaffold: A Novel Nanobiomatrix Platform for Therapeutics Delivery and Bone Regeneration. ACS Appl Mater Interfaces. 2015;715:8088–98.
41. Jing X, Mi H-Y, Wang X-C, Peng X-F, Turng L-S. Shish-Kebab-Structured Poly(ε-Caprolactone) Nanofibers Hierarchically Decorated with Chitosan–Poly(ε-Caprolactone) Copolymers for Bone Tissue Engineering. ACS Appl Mater Interfaces. 2015;712:6955–65.
42. Tarafder S, Bose S. Polycaprolactone-Coated 3D Printed Tricalcium Phosphate Scaffolds for Bone Tissue Engineering: *In Vitro* Alendronate Release Behavior and Local Delivery Effect on *In Vivo* Osteogenesis. ACS Appl Mater Interfaces. 2014;613:9955–65.
43. Gao X, Song J, Ji P, Zhang X, Li X, Xu X, et al. Polydopamine-Templated Hydroxyapatite Reinforced Polycaprolactone Composite Nanofibers with Enhanced Cytocompatibility and Osteogenesis for Bone Tissue Engineering. ACS Appl Mater Interfaces. 2016;85:3499–515.
44. Chang MC, Ko C-C, Douglas WH. Conformational change of hydroxyapatite/gelatin nanocomposite by glutaraldehyde. Biomaterials. 2003;2418:3087–94.
45. Woodruff MA, Hutmacher DW. The return of a forgotten polymer—Polycaprolactone in the 21st century. Progress Polymer Sci. 2010;3510:1217–56.
46. Zhao Y, Peng X, Wang D, Zhang H, Xin Q, Wu M, et al. Chloroplast-inspired Scaffold for Infected Bone Defect Therapy: Towards Stable Photothermal Properties and Self-Defensive Functionality. Adv Sci (Weinh). 2022;931:e2204535.
47. Qin C, Ma J, Chen L, Ma H, Zhuang H, Zhang M, et al. 3D bioprinting of multicellular scaffolds for osteochondral regeneration. Materials Today. 2021;49:68–84.
48. Ma L, Wang X, Zhou Y, Ji X, Cheng S, Bian D, et al. Biomimetic Ti-6Al-4V alloy/gelatin methacrylate hybrid scaffold with enhanced osteogenic and angiogenic capabilities for large bone defect restoration. Bioact Mater. 2021;610:3437–48.
49. Wang L, Zhu T, Kang Y, Zhang J, Du J, Gao H, et al. Crimped nanofiber scaffold mimicking tendon-to-bone interface for fatty-infiltrated massive rotator cuff repair. Bioact Mater. 2022;16:149–61.
50. Xia Y, Fan X, Yang H, Li L, He C, Cheng C, et al. ZnO/Nanocarbons-Modified Fibrous Scaffolds for Stem Cell-Based Osteogenic Differentiation. Small. 2020;1638:e2003010.
51. Gu J, Zhang Q, Geng M, Wang W, Yang J, Khan AUR, et al. Construction of nanofibrous scaffolds with interconnected perfusable microchannel networks for engineering of vascularized bone tissue. Bioact Mater. 2021;610:3254–68.
52. Luo H, Zhang Y, Wang Z, Yang Z, Tu J, Liu Z, et al. Constructing three-dimensional nanofibrous bioglass/gelatin nanocomposite scaffold for enhanced mechanical and biological performance. Chem Eng J. 2017;326:210–21.
53. Nichol JW, Koshy ST, Bae H, Hwang CM, Yamanlar S, Khademhosseini A. Cell-laden microengineered gelatin methacrylate hydrogels. Biomaterials. 2010;3121:5536–44.
54. Cabral CSD, Miguel SP, de Melo-Diogo D, Louro RO, Correia IJ. Green reduced graphene oxide functionalized 3D printed scaffolds for bone tissue regeneration. Carbon. 2019;146:513–23.
55. Li X, Zou Q, Chen H, Li W. *In vivo* changes of nanoapatite crystals during bone reconstruction and the differences with native bone apatite. Sci Adv. 2019;5:eaay6484.
56. Lohmann CH, Dean DD, Koster G, Casasola D, Buchhorn GH, Fink U, et al. Ceramic and PMMA particles differentially affect osteoblast phenotype. Biomaterials. 2002;23:1855–63.
57. Pei DD, Sun JL, Zhu CH, Tian FC, Jiao K, Anderson MR, et al. Contribution of Mitophagy to Cell-Mediated Mineralization: Revisiting a 50-Year-Old Conundrum. Adv Sci (Weinh). 2018;510:1800873.
58. Liu B, Liu J, Wang C, Wang Z, Min S, Wang C, et al. High temperature oxidation treated 3D printed anatomical WE43 alloy scaffolds for repairing periarticular bone defects: *In vitro* and *in vivo* studies. Bioact Mater. 2024;32:177–89.
59. Li C, Sun F, Tian J, Li J, Sun H, Zhang Y, et al. Continuously released Zn2+ in 3D-printed PLGA/β-TCP/Zn scaffolds for bone defect repair by improving osteoinductive and anti-inflammatory properties. Bioact Mater. 2023;24:361–75.
60. Wang L, Qiu Y, Lv H, Si Y, Liu L, Zhang Q, et al. 3D Superelastic Scaffolds Constructed from Flexible Inorganic Nanofibers with Self-Fitting Capability and Tailorable Gradient for Bone Regeneration. Adv Funct Mater. 2019;29(31):1901407.
61. Dwivedi R, Kumar S, Pandey R, Mahajan A, Nandana D, Katti DS, et al. Polycaprolactone as biomaterial for bone scaffolds: Review of literature. Journal of Oral Biology and Craniofacial Research. 2020;101:381–8.
62. Ha Y, Ma X, Li S, Li T, Li Z, Qian Y, et al. Bone Microenvironment-Mimetic Scaffolds with Hierarchical Microstructure for Enhanced Vascularization and Bone Regeneration. Adv Funct Mater. 2022;32(20):2200011.

63. Li J, Wang C, Gao G, Yin X, Pu X, Shi B, et al. MBG/ PGA-PCL composite scaffolds provide highly tunable degradation and osteogenic features. Bioact Mater. 2022;15:53–67.
64. Zhang Q, Ma L, Ji X, He Y, Cui Y, Liu X, et al. High-Strength Hydroxyapatite Scaffolds with Minimal Surface Macrostructures for Load-Bearing Bone Regeneration. Adv Funct Mater. 2022;32(33):2204182.
65. Vu AA, Burke DA, Bandyopadhyay A, Bose S. Effects of surface area and topography on 3D printed tricalcium phosphate scaffolds for bone grafting applications. Additive Manufacturing. 2021;39:101870.
66. Huang Y, Onyeri S, Siewe M, Moshfeghian A, Madihally SV. *In vitro* characterization of chitosan-gelatin scaffolds for tissue engineering. Biomaterials. 2005;2636:7616–27.

Publisher's Note